Axion Electrodynaimcs: Theoretical Treatment of Dielectric and Simulation of Cavity Haloscopes

King's College London

7CCP1500

Author: Wong Siu Tung
Supervisor: Dr. David Marsh

April 26, 2024

Abstract

A successful attempt at capturing the physic behind axion-induced electric field resonating with an applied electric field; the thesis starts with derivation for the axion-maxwell's equations, linearised then simplified for numerical simulations. The thesis provided theoretical background for dielectric haloscopes and numerical results for cavity haloscopes. The result simulation shows excellent promise in extracting the physics of resonances but falls short of delivering an accurate result relative to experimental observations.

Contents

Chapter 1

Introduction

(The introduction section is directly paraphrased from the literature review)
Dark matter is one of the fundamental components of the universe, accounting for approximately 27% of its total energy density. Unlike ordinary matter, dark matter does not emit, absorb, or reflect light, making it detectable only through its gravitational interactions with visible matter. These interactions play a critical role in the formation and structure of galaxies, influencing their rotational speeds and distribution within clusters. The existence of dark matter is pivotal for understanding the large-scale structure of the cosmos and the dynamics of cosmic expansion.

Among the hypothetical particles proposed as dark matter candidates, axions are particularly intriguing due to their potential to also solve the strong CP problem in quantum chromodynamics (QCD). This problem arises from the non-observation of CP violation in the strong interactions, which is unexpected given the QCD Lagrangian's potential for such violations. Axions were proposed by Peccei and Quinn as a byproduct of a new symmetry, now known as the Peccei-Quinn symmetry, which naturally suppresses CP violation in strong interactions. The axion is thus a pseudo-Goldstone boson resulting from the spontaneous breaking of this symmetry.

The detection of axions, however, poses significant experimental challenges due to their weakly interacting nature. Cavity haloscopes represent one of the most promising approaches for detecting axion dark matter, especially for axions with masses in the microelectronvolt (μeV) range. These devices utilize a resonant cavity that enhances the axion-photon conversion process in the presence of a strong magnetic field.

Dielectric haloscopes like MADMAX extend the detection possibilities to axions with higher masses. These devices employ multiple layered dielectric disks within a magnetic field to boost the conversion efficiency of axions into detectable photons. The setup capitalizes on constructive interference from electromagnetic waves generated at the interfaces of these disks. The principle of operation for dielectric haloscopes is based on the axion-induced changes in the electric field across these interfaces, which can be enhanced by precisely tuning the spacing between the disks to match the wavelength corresponding to the axion mass. This strategy allows for a broader search range and potentially higher sensitivity compared to cavity haloscopes.

The power conversion in dielectric haloscopes can be influenced by the disk material, spacing, and overall design, which are optimized to maximize constructive interference and thus enhance the signal strength. This method is particularly suited for scanning a wide range of axion masses quickly, making it invaluable for axion dark matter searches that aim to cover a broad spectrum of possible axion masses.

Both cavity and dielectric haloscopes are at the forefront of the experimental search for dark matter axions. These approaches not only highlight the diverse methodologies in dark matter research but also underscore the profound implications such discoveries would have on our understanding of the universe's fundamental makeup.

Chapter 2

Theory

2.1 Deriving Axion-Maxwell's and Wave Equations

The Lagrangian density that describes the interaction between photons, axions, and electromagnetic (EM) currents is given by

$$\mathcal{L} = -\frac{1}{4}F_{\mu\nu}F^{\mu\nu} - J_\mu A^\mu + \frac{1}{2}\partial_\mu\phi\partial^\mu\phi - \frac{1}{2}m_\phi^2\phi^2 - \frac{g_{\phi\gamma}}{4}F_{\mu\nu}\tilde{F}^{\mu\nu}\phi, \tag{2.1}$$

where ϕ is the axion field, m_ϕ is the axion mass, $g_{\phi\gamma}$ is the axion photon coupling constant given in units of inverse energy; $F_{\mu\nu} = \partial_\mu A_\nu - \partial_\nu A_\mu$ is the EM field-strength tensor; It is given in terms of the vector potential $A^\mu = (A_0, \mathbf{A})$, and $J^\mu = (\phi, \mathbf{J})$ is the electric 4-current. $\tilde{F}^{\mu\nu} = \frac{1}{2}\epsilon^{\mu\nu\alpha\beta}F_{\alpha\beta}$ is the dual tensor where $\epsilon^{0123} = \epsilon^{123} = +1$. The magnetic and electric fields are represented explicitly as

$$\mathbf{E} = -\nabla A_0 - \dot{\mathbf{A}} \ \text{ and } \ \mathbf{B} = \nabla \times \mathbf{A} \,. \tag{2.2}$$

To obtain the axion modified Maxwell's equations, first applying the Euler-Lagrange equation to equation (2.1), with respect to the axion field ϕ and $\partial_\mu\phi$

$$\frac{\partial}{\partial\phi}\mathcal{L}(\phi, \partial_\mu\phi) = \partial_\mu\left(\frac{\partial}{\partial(\partial_\mu\phi)}\mathcal{L}(\phi, \partial_\mu\phi)\right), \tag{2.3}$$

$$\rightarrow \frac{\partial}{\partial\phi}\mathcal{L} = -m_\phi^2 - \frac{g_{\phi\gamma}}{4}F_{\mu\nu}\tilde{F}^{\mu\nu} \ \text{ E.q.1}$$

$$\rightarrow \frac{\partial}{\partial(\partial_\mu\phi)}\mathcal{L} = \frac{\partial}{\partial(\partial_\mu\phi)}\left(\frac{1}{2}\partial_\mu\phi\partial^\mu\phi\right)$$

$$= \frac{\partial}{\partial(\partial_\mu\phi)}\left(\frac{1}{2}\eta^{\nu\mu}\partial_\mu\partial_\nu\phi\right) = \frac{1}{2}\eta^{\nu\mu}\left(\frac{\partial}{\partial(\partial_\mu\phi)}[\partial_\mu\phi]\partial_\nu\phi + \partial_\mu\phi\frac{\partial}{\partial(\partial_\mu\phi)}[\partial_\nu\phi]\right)$$

$$= \frac{1}{2}\eta^{\nu\mu}\left(\delta_\mu^\mu\partial_\nu\phi + \partial_\mu\phi\delta_\nu^\mu\right) = \frac{1}{2}\eta^{\nu\mu}\left(\partial_\nu\phi + \partial_\nu\phi\right) = \eta^{\nu\mu}\partial_\nu\phi = \partial^\mu\phi \ \text{ E.q.2}$$

$$\text{E.q.1} = \text{E.q.2} \Rightarrow (\partial_\mu\partial^\mu + m_\phi^2)\phi = -\frac{g_{\phi\gamma}}{4}F_{\mu\nu}\tilde{F}^{\mu\nu}, \tag{2.4}$$

$$\frac{\partial}{\partial A_\mu}\mathcal{L}(A_\mu, \partial_\mu A_\nu) = \partial_\nu\left(\frac{\partial}{\partial(\partial_\omega A_\rho)}\mathcal{L}(A_\mu, \partial_\mu A_\nu)\right) \tag{2.5}$$

$$\Rightarrow \frac{\partial}{\partial A_\mu}\mathcal{L} = -J^\mu \ \text{ E.q.1}$$

$$\Rightarrow \partial_\nu\left(\frac{\partial}{\partial(\partial_\omega A_\rho)}\mathcal{L}\right) = \partial_\nu\left(\frac{\partial}{\partial(\partial_\omega A_\rho)}\left[-\frac{1}{4}F_{\mu\nu}F^{\mu\nu} - \frac{g_{\phi\gamma}}{4}F_{\mu\nu}\tilde{F}^{\mu\nu}\phi\right]\right)$$

$$= \frac{\partial}{\partial(\partial_\omega A_\rho)}\left[-\frac{1}{4}\eta^{\mu\alpha}\eta^{\nu\beta}F_{\mu\nu}F^{\mu\nu} - \frac{g_{\phi\gamma}}{4}\frac{\epsilon^{\mu\nu\alpha\beta}}{2}F_{\mu\nu}F_{\alpha\beta}\phi\right]$$

$$= -\frac{1}{4}\eta^{\mu\alpha}\eta^{\nu\beta}\left(\left[\delta^\omega_\mu\delta^\rho_\nu - \delta^\omega_\nu\delta^\rho_\mu\right]F_{\alpha\beta} + F_{\mu\nu}\left[\delta^\omega_\alpha\delta^\rho_\beta - \delta^\omega_\beta\delta^\rho_\alpha\right]\right)$$

$$-\frac{g_{\phi\gamma}}{4}\frac{\epsilon^{\mu\nu\alpha\beta}}{2}\phi\left(\left[\delta^\omega_\mu\delta^\rho_\nu - \delta^\omega_\nu\delta^\rho_\mu\right]F_{\alpha\beta} + F_{\mu\nu}\left[\delta^\omega_\alpha\delta^\rho_\beta - \delta^\omega_\beta\delta^\rho_\alpha\right]\right)$$

$$= -F^{\mu\nu} - g_{\phi\gamma}\tilde{F}^{\mu\nu}\phi$$

$$\Rightarrow -\partial_\nu F^{\mu\nu} - g_{\phi\gamma}\partial_\nu(\tilde{F}^{\mu\nu}\phi) \;\; \text{E.q.2} \;; \partial_\nu(\tilde{F}^{\mu\nu}\phi) = \partial_\nu(\tilde{F}^{\mu\nu})\phi + \tilde{F}^{\mu\nu}\partial_\nu(\phi) = \tilde{F}^{\mu\nu}\partial_\nu\phi$$

$$\text{E.q.1} = \text{E.q.2} \Rightarrow \partial_\nu F^{\mu\nu} = J^\mu - g_{\phi\gamma}\tilde{F}^{\mu\nu}\partial_\nu\phi \;. \tag{2.6}$$

Equation 2.6 represents the modification of Gauss and Ampère's laws in the presence of axion fields, resulting in the additional current term; additionally, the step before equation 2.6, the Bianchi identity allows for $\partial_\mu\tilde{F}^{\mu\nu} = 0$. Executing the repeated indices in equations 2.4 and 2.6 results in five equations

$$\nabla \cdot \mathbf{E} = \rho - g_{\phi\gamma}\mathbf{B}\cdot\phi, \tag{2.7}$$
$$\nabla \times \mathbf{B} - \dot{\mathbf{E}} = \mathbf{J} + g_{\phi\gamma}(\mathbf{B}\dot{\phi} - \mathbf{E}\times\nabla\phi), \tag{2.8}$$
$$\nabla \cdot \mathbf{B} = 0, \tag{2.9}$$
$$\nabla \times \mathbf{E} + \dot{\mathbf{B}} = 0, \tag{2.10}$$
$$\ddot{\phi} - \nabla^2\phi + m_\phi^2\phi = g_{\phi\gamma}\mathbf{E}\cdot\mathbf{B} \;. \tag{2.11}$$

Equations 2.7 to 2.11 are th the basis for this thesis. They will be used to derive the boundary condition for interfaces. Through rearrangement and substitution, the equations can be written as a wave equation; this will be used as the foundation for the numerical simulation, where the axion acts as a driving frequency.

To arrive at the wave equation, we need to make some approximations; in the context of cold dark matter, the term $\nabla\phi\,(\text{t}, \vec{x})$ is often neglected because it describes the gradient of the axion field, which is a vector field indicating the rate and direction of the quickest increase of the scalar field at any particular location in space. Since the de Broglie wavelength of the axion is considerably larger than the scale of most experiments designed to detect them. This simplification permits the scalar field ϕ to be expressed approximately as $\phi \approx \phi_0 e^{-i\omega_\phi t}$, where $\phi_0 = \sqrt{2\rho_\phi\hbar c^3}/\omega_a$ represents the amplitude of the field, given in terms of the local dark matter density and ω_ϕ represents the frequency which is linked to the axion's mass by the relationship $\omega_\phi \approx m_\phi c^2/\hbar$. The axion photon interaction is given by $g_{\phi\gamma} = (g_\gamma\alpha/\pi)\sqrt{s\rho_\phi\hbar^3 c^3/\chi}$, where $g_{\phi\gamma}\phi_0 \ll 1$. Therefor, equation 2.7 to 2.10 can be rewritten as

$$\nabla \cdot \mathbf{E} = \rho - g_{\phi\gamma}\mathbf{B}\cdot\phi \approx 0, \tag{2.12}$$
$$\nabla \times \mathbf{B} - \dot{\mathbf{E}} \approx i\omega_\phi(g_{\phi\gamma}\phi_0 e^{-i\omega_\phi t})\mathbf{B}_0, \tag{2.13}$$
$$\nabla \cdot \mathbf{B} = 0, \tag{2.14}$$
$$\nabla \times \mathbf{E} + \dot{\mathbf{B}} = 0 \;. \tag{2.15}$$

In equations 2.12 and 2.13, the charge density in a haloscope is approximately zero, thus implying a zero current as well ($\rho = 0 \Rightarrow \mathbf{J} = 0$) [6].

From equations 2.12 to 2.15 we can now derive the wave equation with some driving frequency

$$\nabla \times (\nabla \times \mathbf{E}) = -\frac{\partial}{\partial t}(\nabla \times \mathbf{B}) \tag{2.16}$$

$$= -\frac{\partial}{\partial t}\left(\dot{\mathbf{E}} + i\omega_\phi\left(g_{\phi\gamma}\phi_0 e^{-\omega_\phi t}\right)\mathbf{B}_0\right)$$

$$= -\frac{\partial}{\partial t}\left(\dot{\mathbf{E}} + i\omega_\phi g_{\phi\gamma}\phi_0\mathbf{B}_0\left[\cos\left(\omega_\phi t\right) - i\sin\left(\omega_\phi t\right)\right]\right)$$

$$\nabla(\nabla\cdot\mathbf{E}) - \nabla^2\mathbf{E} = -\ddot{\mathbf{E}} + \omega_\phi g_{\phi\gamma}\phi_0\mathbf{B}_0\frac{\partial}{\partial t}\left(\Re\left[i\cos\left(\omega_\phi t\right) + \sin\left(\omega_\phi t\right)\right]\right)$$

$$-\nabla^2\mathbf{E} = -\ddot{\mathbf{E}} - \omega_\phi g_{\phi\gamma}\phi_0\mathbf{B}\omega_\phi\cos\left(\omega_\phi t\right) . \tag{2.17}$$

Returning the units for equation 2.17 gives us

$$-\nabla^2\mathbf{E} = -\mu\epsilon\ddot{\mathbf{E}} - \frac{\omega_\phi^2\mu}{Z_0}g_{\phi\gamma}\phi_0\mathbf{B}\cos\left(\omega_\phi t\right) . \tag{2.18}$$

Observe that equation 2.18 is in the form of a wave equation with some driving frequency; thus, solving it will provide us with the electric field under the influence of a sinusoidal axion field for a specific geometry. We will return to equation 2.18 in Chapter 3. Thus, let's focus on the boundary condition of EM waves.

2.2 Boundary Conditions for Axion Induced EM Waves

2.2.1 Linearization of Axion-Maxwell's Equations

We want to formulate Maxwell's equations in the presence of a macroscopic field to account for the EM response to some background medium. As mentioned by Alexander J. Millar [9], for the case of small momentum transfers, it is reasonable to assume the axion filed as a macroscopic field rather than a microscopic field (Certain cases, such as searching for solar axions with Bragg scattering of crystals can be considered as microscopic interaction [3]). Following equations 2.7, 2.8 and 2.11, they can be rewritten with a bounded and free part for the charge and current density, $\rho = \rho_b + \rho_f$ and $\mathbf{J} = \mathbf{J}_b + \mathbf{J}_f$, where $\rho_b = -\nabla \cdot \mathbf{P}$ and $\mathbf{J}_b = \nabla \times \mathbf{M} + \dot{\mathbf{P}}$. Moreover, we will also use the general definition for displacement and magnetisation to represent the macroscopic electric and magnetic field

$$\mathbf{D} = \mathbf{E} + \mathbf{P} \quad \text{and} \quad \mathbf{H} = \mathbf{B} - \mathbf{M}, \tag{2.19}$$

$$\nabla \cdot \mathbf{D} = \rho_f - g_{\phi\gamma}\mathbf{B}\cdot\nabla\phi, \tag{2.20}$$

$$\nabla \times \mathbf{H} - \dot{\mathbf{D}} = \mathbf{J}_f + g_{\phi\gamma}(\mathbf{B}\dot{a} - \mathbf{E}\times\nabla\phi), \tag{2.21}$$

$$\ddot{\phi} - \nabla^2\phi + m_\phi^2 = g_{\phi\gamma}\mathbf{E}\cdot\mathbf{B} . \tag{2.22}$$

To linearise the fields, a static external magnetic field $\mathbf{B}_e$ has been set up by means of an external current $\mathbf{J}_e$; the field $\mathbf{B}_e$ is much stronger than any other field, therefore on the RHS of equation 2.21, $\mathbf{J}_f + g_{\phi\gamma}(\mathbf{B}\dot{a} - \mathbf{E}\times\nabla\phi) \approx \mathbf{J}_f + g_{\phi\gamma}(\mathbf{B}_e\dot{\phi})$. Applying a time derivative to equation 2.21, with the approximation and using the continuity equation ($\dot{\rho}_f = -\nabla\cdot\mathbf{J}_f$), will return

$$\frac{d}{dt}(\nabla\cdot\mathbf{D} - \rho_f) = \frac{d}{dt}(-g_{\phi\gamma}\mathbf{B}_e\cdot\nabla\phi) \tag{2.23}$$

$$\nabla\cdot\mathbf{D} + \nabla\cdot\mathbf{J}_f = -g_{\phi\gamma}\mathbf{B}_e\cdot\nabla\frac{d}{dt}(\phi)$$

$$\nabla(\dot{\mathbf{D}} + \mathbf{J}_f) = -g_{\phi\gamma}\mathbf{B}_e\cdot\nabla\dot{\phi} \tag{2.24}$$

6

Now, taking equations 2.24, 2.21 and 2.22 and representing them in Fourier space using the relations

$$\hat{A}(\omega, \mathbf{K}) = \int d^3x dt e^{i(\omega t - \mathbf{k} \cdot \mathbf{x})} A(t, \mathbf{x}) \tag{2.25}$$

$$\frac{d}{dt}\hat{A} = F\left[\frac{d}{dt}A(t, \mathbf{x})\right] = \int d^3x dt \left[\frac{d}{dt}A(t, \mathbf{x})\right] e^{i(\omega t - \mathbf{k} \cdot \mathbf{x})}$$

$$= \int \left(\left[e^{i(\omega t - \mathbf{k} \cdot \mathbf{x})}A(t, \mathbf{x})\right]_{-\infty}^{\infty} - \int_{-\infty}^{\infty} i\omega e^{i(\omega t - \mathbf{k} \cdot \mathbf{x})}A(t, \mathbf{x})dt\right)d^3x$$

$$= -i\omega\hat{A}(\omega, \mathbf{k}), \tag{2.26}$$

$$\nabla \cdot \hat{A} = \int \left(\left[e^{i(\omega t - \mathbf{k} \cdot \mathbf{x})}A(t, \mathbf{x})\right]_{-\infty}^{\infty} + \int_{-\infty}^{\infty} i\mathbf{k}e^{i(\omega t - \mathbf{k} \cdot \mathbf{x})}A(t, \mathbf{x})d^3x\right)dt$$

$$= i\mathbf{k}\hat{A}(\omega, \mathbf{k}). \tag{2.27}$$

Therefore it is obvious to see how the macroscopic Maxwell's equations will appear in Fourier space

$$\nabla \cdot \left(\frac{d}{dt}\hat{\mathbf{D}} + \hat{\mathbf{J}}_f\right) = -g_{\phi\gamma}\mathbf{B}_e \cdot \nabla\left(\frac{d}{dt}\hat{\phi}\right)$$

$$\omega\mathbf{k} \cdot \hat{\mathbf{D}} + i\mathbf{k} \cdot \hat{\mathbf{J}}_f = g_{\phi\gamma}i\omega\mathbf{B}_e(i\mathbf{k} \cdot \hat{\phi})$$

$$\mathbf{k} \cdot (\omega\hat{\mathbf{D}} + i\hat{\mathbf{J}}_f) = -g_{\phi\gamma}\omega\mathbf{k} \cdot (\mathbf{B}_e\hat{\phi}), \tag{2.28}$$

$$\nabla \times \hat{\mathbf{H}} - \frac{d}{dt}\hat{\mathbf{D}} - \hat{\mathbf{J}}_f = g_{\phi\gamma}\mathbf{B}_e\frac{d}{dt}\hat{\phi}$$

$$i(\mathbf{k} \times \hat{\mathbf{H}}) + i\omega\hat{\mathbf{D}} - \hat{\mathbf{J}}_f = g_{\phi\gamma}(-i\omega\mathbf{B}_e\hat{\phi})$$

$$\mathbf{k} \times \hat{\mathbf{H}} + \omega\hat{\mathbf{D}} + i\hat{\mathbf{J}}_f = -g_{\phi\gamma}\omega\mathbf{B}_e\hat{\phi}, \tag{2.29}$$

$$\frac{d^2}{dt^2}\hat{\phi} - \nabla^2\phi + m_\phi^2 = g_{\phi\gamma}\hat{\mathbf{E}} \cdot \mathbf{B}_e$$

$$(\omega^2 - |\mathbf{k}|^2 - m_a^2)\hat{\phi} = -g_{\phi\gamma}\hat{\mathbf{E}} \cdot \mathbf{B}_e. \tag{2.30}$$

For a homogeneous and isotropic conductive material with a linear response medium, the magnetisation $\mathbf{M} = 0 \Rightarrow \hat{\mathbf{H}} = \hat{\mathbf{B}}/\mu$, $\hat{\mathbf{J}}_f = \sigma\hat{\mathbf{E}}$ and $\hat{\mathbf{P}} = \chi\hat{\mathbf{E}}$ where σ is the conductivity, χ the electric susceptibility, where the total dielectric permittivity is

$$\epsilon = 1 + \chi + \frac{i\sigma}{\omega}. \tag{2.31}$$

The imaginary component of ϵ and χ accounts for the losses caused by the displacement current represented by the axion field, for a perfect conductor $\text{Im}(\epsilon) \approx \sigma/\omega \to \infty$ or for a perfect dielectric $\text{Im}(\epsilon) = 0$, therefore the linearised macroscopic axion-Maxwell's equations in Fourier space can be written as

$$\epsilon\mathbf{k} \cdot \hat{\mathbf{E}} = -g_{\phi\gamma}\mathbf{k} \cdot \mathbf{B}_e\hat{\phi}, \tag{2.32}$$

$$\mathbf{k} \times \hat{\mathbf{H}} + \omega\epsilon\hat{\mathbf{E}} = -g_{\phi\gamma}\omega\mathbf{B}_e\hat{\phi}, \tag{2.33}$$

$$\mathbf{k} \cdot \hat{\mathbf{B}} = 0, \tag{2.34}$$

$$\mathbf{k} \times \hat{\mathbf{E}} - \omega\hat{\mathbf{B}} = 0, \tag{2.35}$$

$$(\omega^2 - |\mathbf{k}|^2 - m_a^2)\hat{\phi} = -g_{\phi\gamma}\hat{\mathbf{E}} \cdot \mathbf{B}_e. \tag{2.36}$$

From here on, we will be working in Fourier space (unless specifically stated), thus the hat notation can be removed for convenience.

2.2.2 Imperfect Dielectric and Axion Energy Expectations

Most real-life dielectric materials used for experiments are not perfect. The EM waves interacting with them would have most of their energy reflected, but a certain amount is also absorbed; thus, stacking multiple layers of dielectrics together may become counterproductive. This loss is quantified through the dielectric loss tangent

$$\tan(\delta) = \frac{\text{Im}(\epsilon)}{\text{Re}(\epsilon)}. \tag{2.37}$$

In a realistic experiment, the dielectric material used would have $\tan(\delta) \ll 1$.

For non-relativistic galactic dark matter axions where the velocity is approximately $v_\phi \leq 10^{-3}\ \text{ms}^{-1}$ and an axion mass in the range of $100\mu\text{eV}$, thus the de Broglie wavelength for axions is of order 10 meters; for a cavity of scale 0.6 meters, the axion field would appear to be homogeneous (this explicitly shows the approximation to derive equation 2.13 is valid for galactic axions). In the limit, as the axion velocity goes to zero, the axion field will be purely time-dependent

$$\phi(\mathbf{v}, t) = \phi_0 e^{-it(m_\phi - \mathbf{k}\cdot\mathbf{v})} \xrightarrow[\lim v=0]{} \phi_0 e^{-im_\phi t}\ ; \omega = m_\phi \tag{2.38}$$

The axion field strength ϕ_0 governs the local axion dark matter density

$$\rho_a = \frac{m_\phi^2 |\phi_0|^2}{2} = f_{DM} \frac{300\text{MeV}}{\text{cm}^3}. \tag{2.39}$$

Where f_{DM} represents the uncertainty in the local dark matter density and the fraction of dark matter made up of axions relative to other possible forms of dark matter.

For low axion momentum, $\mathbf{k}_\phi \approx 0$, we can directly read off equation 2.33, arrive at an equation to describe the homogeneous axion-induced electric field

$$\mathbf{E}_\phi(t) = -\frac{g_{\phi\gamma}\mathbf{B}_e}{\epsilon}\phi(t) \tag{2.40}$$

$$\mathbf{E}_\phi(t) = -\frac{\mathbf{E}_0}{\epsilon}e^{-im_\phi t} \tag{2.41}$$

$$\mathbf{E}_0 \equiv g_{\phi\gamma}\mathbf{B}_e\phi_0. \tag{2.42}$$

To represent equation 2.42 numerically and provide some intuition for the energy scales we are working with

$$|\mathbf{E}_0| = |g_{\phi\gamma}\mathbf{B}_e\phi_0| \tag{2.43}$$

$$g_{\phi\gamma} = -2.04 \times 10^{-16}\text{GeV}^{-1}\left(\frac{m_\phi}{1\mu\text{eV}}\right)C_{\phi\gamma}\ ; \phi_0 = \left(\frac{f_{DM} \times 600\text{MeV}}{m_\phi^2\text{cm}^3}\right)^{1/2} \tag{2.44}$$

$$\mathbf{E}_0 = 1.3 \times 10^{-12}\text{V/m}\frac{B_e}{10\text{T}}|C_{\phi\gamma}|f_{DM}^{1/2}, \tag{2.45}$$

with a typical home electric outlet being approximately 12000 V/m; an axion-induced EM field is approximately $9.7 \times 10^{-13}\text{V/m}$, this is a difference in the order of 10^{16} ! For an analogy analogy, if a human took up a space of 1 meter, 10^{16} meters would be a light year or the average size of a nebula; this is why the axion is very difficult to detect!

2.2.3 Radiation from an Interface

(Comment: I will use $E_{1,2}^{\gamma;\phi}$ for fields in both regions, while $E_{\gamma,\phi}$ is for a particular field.)

A simple example of an infinite plane between two regions, under a uniform magnetic field $\mathbf{B}_e$ aligned parallel to the interface, as illustrated in figure 2. This interface exhibits discontinuities in either the dielectric constant ϵ, the magnetic field $\mathbf{B}_e$, or both, leading to a discontinuous axion-induced electric field $\mathbf{E}_1^\phi$ and $\mathbf{E}_2^\phi$ across the interface. Each region individually satisfies the axion-Maxwell's equations (the solution is given as a sum of the general solution to EM waves and $\mathbf{E}_\phi$); therefore, a global solution results in choosing a field in region 1 and 2 such that the boundary conditions are satisified. This arrangement effectively links the axion-induced electric field with the electromagnetic waves that propagate away from the interface in perpendicular directions. We ignore sources of EM waves from far away and assume there is no "noise" to the axion field (EM waves unrelated to the perpendicular propagation and the axion field).

The axion induced electric field ($\mathbf{E}_\phi$), electric ($\mathbf{E}_\gamma$) and magnetic ($\mathbf{H}_\gamma$) fields are strictly parallel to the interface. The typical continuity conditions at the interface between different media require that the components of the electric field $E_\parallel$ and the magnetic field $H_\parallel$ are equal at the boundary.
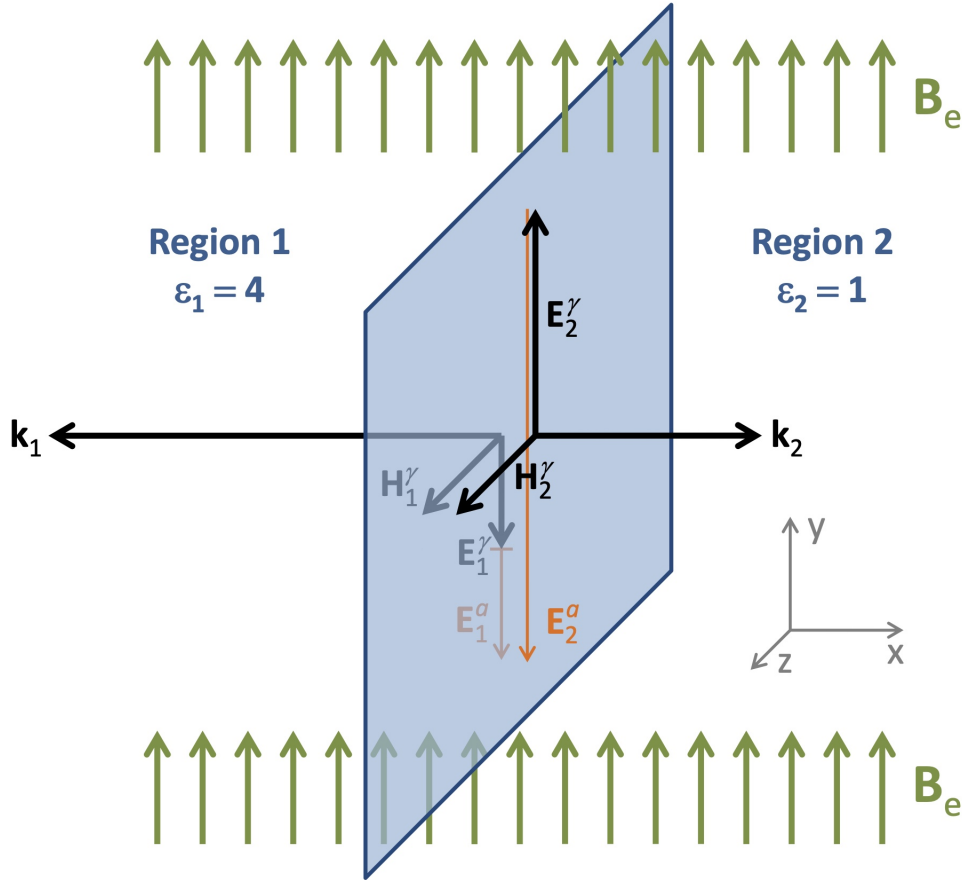

Figure 2.1: Boundary between two regions (labelled 1 and 2) with identical B_e and specified material properties, where $\mu_1 = \mu_2 = 1$, $\epsilon_1 = 4$, and $\epsilon_2 = 1$. This setup yields the resrfractive index of $n_1 = \sqrt{\epsilon_1} = 2$ and $n_2 = 1$, leading to wave numbers $k_1 = 2\omega$ and $k_2 = \omega$. The emitted electromagnetic waves from the interface guarantee the continuity of $H_\parallel$ and $E_\parallel$, resulting in $\mathbf{H}_1^\gamma = \mathbf{H}_2^\gamma = 0.5$, $\mathbf{E}_1^\phi = \mathbf{E}_1^\gamma = -0.25$, $\mathbf{E}_1^\phi = -1$, and $\mathbf{E}_2^\gamma = 0.5$. All field strengths are expressed relative to $E_0 = |g_{\phi\gamma}B_e\phi_0|$. (Image from taken [9], please note that in the image $\mathrm{E}^a \equiv \mathrm{E}^\phi$, this is a difference in notations)

From equation 2.33 without the source term, it follows that the usual relationship $\mathbf{k} \times \mathbf{H}_\gamma + \omega\epsilon\mathbf{E}_\gamma = 0$ holds, where $\mathbf{H}_\gamma$ and $\mathbf{E}_\gamma$ represent the magnetic and electric fields of the propagating electromagnetic wave, respectively. Given that the wave vector satisfies $k = n\omega$, we derive

$$\mathbf{k} \times \mathbf{H}_\gamma + \omega\epsilon\mathbf{E}_\gamma = 0 \tag{2.46}$$

$$(\pm k_{x,1,2}H^\gamma_{z,1,2} \mp \omega\epsilon E^\gamma_{y,1,2})\hat{y} = 0$$

$$H^\gamma_{1,2} = \pm\frac{\omega\epsilon}{k}E_\gamma$$

$$H_\gamma = \pm(\epsilon/n)E_\gamma. \tag{2.47}$$

Since μ and ϵ determine $n = \sqrt{\epsilon\mu}$, the expression simplifies to $\epsilon/n = \sqrt{\epsilon/\mu}$. The setup described by $\mu \approx 1$ simplifies further, allowing us to approximate $n \approx \sqrt{\epsilon}$. It is crucial to note that $\mathbf{H}_\gamma$ is perpendicular to $\mathbf{E}_\gamma$, which aligns with the axion-induced field $\mathbf{E}_\phi$, and therefore, parallel to the magnetic field $\mathbf{B}_e$. Hence, the continuity of $H_\parallel$ involves neither $\mathbf{B}_e$ nor $\mathbf{E}_\gamma$; the continuity of $E_\parallel$ relies on both E_γ and E_ϕ, therefore the continuity condition is given by

$$\text{Continuity of } H_\parallel \quad -\frac{\epsilon_1}{n_1}E^\gamma_1 = -\frac{\epsilon_2}{n_2}E^\gamma_2, \tag{2.48}$$

$$\text{Continuity of } E_\parallel \quad E^\gamma_1 + E^\phi_1 = E^\gamma_2 + E^\phi_2, \tag{2.49}$$

now to rearrange for $E^\gamma_{1,2}$ and $H^\gamma_{1,2}$ such that they are a function of, $E^\phi_{1,2}$, $\epsilon_{1,2}$ and $n_{1,2}$

$$-\frac{\epsilon_1}{n_1}E^\gamma_1 = \frac{\epsilon_2}{n_2}(E^\gamma_1 + E^\phi_1 - E^\phi_2). \tag{2.50}$$

Equation 2.48 is a combination of equations 2.46 and 2.47, where the global $E^\gamma_{1,2}$ wave can be represented in terms of the axion-induced wave and constants relating to the experimental set-up (i.e. refractive index and permittivity); in section 2.3.1, we will discuss the case of multiple regions with varying refractive index and permittivity. For now, let's rewrite equation 2.48 into a more useful form

$$E^\gamma_1 = +(E^\phi_2 - E^\phi_1)\frac{\epsilon_2 n_1}{(\epsilon_1 n_2 + \epsilon_2 n_1)}, \tag{2.51}$$

$$E^\gamma_2 = -(E^\phi_2 - E^\phi_1)\frac{\epsilon_1 n_2}{(\epsilon_1 n_2 + \epsilon_2 n_1)}, \tag{2.52}$$

and using the relation $H_\gamma = \pm(\epsilon/n)E_\gamma$, to obtain

$$H^\gamma_{1,2} = -(E^\phi_2 - E^\phi_1)\frac{\epsilon_1 n_2}{(\epsilon_1 n_2 + \epsilon_2 n_1)}. \tag{2.53}$$

Returning to the dielectric interface shown in Figure 2.1, where $\epsilon_1 \neq \epsilon_2$, $\mu_1 = \mu_2 = 1$, $\epsilon_i = n_i^2$ and $\mathbf{B}_e$ is homogeneous; using equations 2.48 to 2.50 and 2.41, we can arrive at an equation for the energy flux density

$$E_\phi(t = 0) = -\frac{E_0}{\epsilon}, \tag{2.54}$$

$$E^\phi_2 - E^\phi_1 = -\left(\epsilon_2^{-1} - \epsilon_1^{-1}\right)E_0,$$

$$\Rightarrow E^\gamma_1 = -\frac{E_0}{n_1}\left(n_2^{-1} - n_1^{-1}\right) \text{ and } E^\gamma_2 = \frac{E_0}{n_2}\left(n_2^{-1} - n_1^{-1}\right), \tag{2.55}$$

$$H^\gamma_{1,2} = E_0\left(n_2^{-1} - n_1^{-1}\right). \tag{2.56}$$

For complex components, the Poynting vector would be represented as

$$\langle\mathbf{S}\rangle = \frac{1}{2}\text{Re}(\mathbf{E} \times \mathbf{H}^*) \tag{2.57}$$

$$\langle\mathbf{S}^\gamma_i\rangle = \mp\frac{E_0^2}{2n_i}\left(\frac{1}{n_2} - \frac{1}{n_1}\right)^2 \tag{2.58}$$

A positive value of the pointing flux signifies energy flowing in the positive x-direction; the medium with the smallest refractive index carries a larger amount of energy produced in EM waves.

2.2.4 Energy Flux and Detection

Equation 2.58 shows energy being carried away from the interface given by $E^\gamma_{1,2}$ and $H^\gamma_{1,2}$, which are fields that are continuous across the boundary, which appears to violate the conservation of energy. To resolve this issue, we need to recognise that the total electric and magnetic fields at the interface are the superpositions of the axion-induced field and the fields of the propagating EM waves. Therefore, the Pyonting vector must also include the axion-induced field

$$\mathbf{S} = (\mathbf{E}_\phi + \mathbf{E}_\gamma) \times \mathbf{H}_\gamma. \tag{2.59}$$

Thus, the axion-induced field is what caused the "creation" of energy at the boundary, but in reality, it is a redistribution of energy. Now to write out equation 2.59 interns of useful constants

$$E^\phi_{1,2}(t) = \text{Re}\left[E^\phi_{1,2}e^{-i\omega t}\right], \tag{2.60}$$

$$E^\gamma_{1,2}(x,t) = \text{Re}\left[E^\gamma_{1,2}e^{-i(\omega t - k_{1,2}x)}\right], \tag{2.61}$$

$$H^\gamma_{1,2}(x,t) = \text{Re}\left[H^\gamma_{1,2}e^{-i(\omega t - k_{1,2}x)}\right]. \tag{2.62}$$

Assuming real, sinusoidal forms for the EM waves at the boundary where $x = 0$

$$E_\gamma = E_{\gamma 0}\cos(\omega t) \tag{2.63}$$

$$H_\gamma = H_{\gamma 0}\cos(\omega t) \tag{2.64}$$

Cycle-averaged Poynting vector at the interface, assuming $\langle\cos^2(\omega t)\rangle = \frac{1}{2}$,

$$\langle S_i\rangle = \frac{1}{2}\left[E^\gamma_i + E^\phi_i\cos(k_i x)\right]H^\gamma_i, \tag{2.65}$$

substituting equations 2.55 and 2.56 would return

$$\langle S_i\rangle = -\frac{E_0^2}{2n_i}\left(\frac{1}{n_2} - \frac{1}{n_1}\right)\left(\pm\left(\frac{1}{n_2} - \frac{1}{n_1}\right) + \frac{\cos(n_i\omega x)}{n_i}\right). \tag{2.66}$$
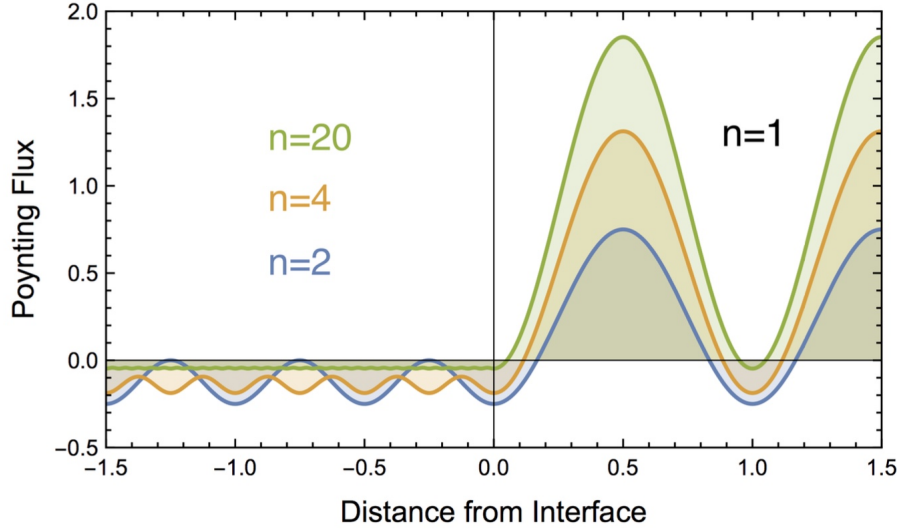

Figure 2.2: The cycle-averaged energy flux density, represented by the Poynting vector in the x-direction, is calculated as $E_0^2/2$ for the configuration depicted in Figure 2. Here, region 1 is positioned at negative x-values and region 2 at positive x-values. The refractive indices for region 1, shown in blue, orange, and green, are set at $n_1 = 2$, 4, and 20, respectively, while n_2 is consistently 1 for region 2. (Image from taken [9])

11

The detection of electromagnetic radiation emitted by a perfect mirror into a vacuum. From equation 2.58, we calculate the cycle-averaged energy flux density, represented as power per unit surface area in the x-direction:

$$\frac{P_\gamma}{A} = \langle S_2^\gamma \rangle = \frac{\langle \text{Re}(E_\gamma^2) \times \text{Re}(H_\gamma^2) \rangle_x}{2} = \frac{E_0^2}{2} = 2.2 \times 10^{-27} \frac{W}{m^2} \left(\frac{B_e}{10\,T} \right)^2 C_{\phi\gamma}^2 f_{DM}. \tag{2.67}$$

The corresponding photon flux is:

$$F_\gamma = \frac{P_\gamma}{A\omega} = \frac{12}{m^2\,\text{day}} \left(\frac{100\mu\text{eV}}{m_\phi} \right) \left(\frac{B_e}{10\,T} \right)^2 C_{\phi\gamma}^2 f_{DM}, \tag{2.68}$$

The flux is notably minimal. Considering that galactic axions exhibit a velocity dispersion around 10^{-3}, the kinetic energy spread of these non-relativistic axions results in a signal bandwidth determined by:

$$\Delta\nu_\phi = \frac{\Delta\omega_\phi}{2\pi} \approx \frac{m_\phi v_\phi^2}{2} \tag{2.69}$$

For a linear amplifier with a system noise T_{sys}, after a measurement duration Δt, the Gaussian noise power fluctuations and the signal-to-noise ratio can be approximated by the Dicke radiometer equation:

$$\frac{S}{N} = \frac{P_\gamma}{T_{sys}} \sqrt{\frac{\Delta t}{\Delta\nu_\phi}} = 1.0 \times 10^{-4} \left(\frac{A}{1\,m^2} \right) \sqrt{\frac{100\,\mu eV}{m_\phi}} \sqrt{\frac{\Delta t}{\text{week}}} \left(\frac{8\,K}{T_{sys}} \right) \left(\frac{B_e}{10\,T} \right)^2 C_{\phi\gamma}^2 f_{DM} \tag{2.70}$$

To detect axion dark matter within a reasonable timescale, an enhancement of the signal power by at least a factor of 10^4 is necessary, achievable through the use of multiple interfaces, thereby defining a boost factor β for the electric-field amplitude:

$$P_\gamma = \frac{\beta^2 E_0^2}{2} \eta \tag{2.71}$$

This setup requires a specific signal-to-noise ratio S/N in a given search channel $\Delta\nu_\phi$, influencing the scanning speed per channel.

2.3 Theoretical Calculations of Dielectric Boosts

2.3.1 Transfer Matrix Formalism

The transfer matrix formalism [13] is a mathematical tool for analysing the propagation and scattering of waves through different media. The transfer matrix connects the state of a wave at one point to its state at another. For example, consider a system of layers, each with its dielectric permittivity ϵ and magnetic permeability μ. Assume a plane wave solution where the wave vector is partly normal to the layer interfaces.

For a given layer j, the electromagnetic field can be decomposed into forward and backward propagating waves. The electric field $\mathbf{E}$ and the magnetic field $\mathbf{H}$ in a layer j can be expressed as:

$$\mathbf{E}_j(z) = \mathbf{E}_{j+}e^{ik_{jz}z} + \mathbf{E}_{j-}e^{-ik_{jz}z} \tag{2.72}$$

$$\mathbf{H}_j(z) = \mathbf{H}_{j+}e^{ik_{jz}z} + \mathbf{H}_{j-}e^{-ik_{jz}z} \tag{2.73}$$

where k_{jz} is the component of the wave vector in the z-direction for the jth layer.

At each interface, the tangential components of the electric and magnetic fields must be continuous. This provides the boundary conditions:

$$\mathbf{E}_j(z_j) = \mathbf{E}_{j+1}(z_j) \tag{2.74}$$

$$\mathbf{H}_j(z_j) = \mathbf{H}_{j+1}(z_j) \tag{2.75}$$

where z_j is the position of the j-th interface.

These boundary conditions can be expressed in matrix form by defining field vectors and a transfer matrix for each layer:

$$\begin{bmatrix} E_{j+1}^+ \\ E_{j+1}^- \end{bmatrix} = \mathbf{T}_j \begin{bmatrix} E_j^+ \\ E_j^- \end{bmatrix} \tag{2.76}$$

$$\mathbf{T}_j = \begin{bmatrix} t_{11} & t_{12} \\ t_{21} & t_{22} \end{bmatrix} \tag{2.77}$$

The elements of $\mathbf{T}_j$ are derived from the boundary conditions and the specific properties (like permittivity and permeability) of the layer j.

For a multilayer system, the overall effect is given by the product of the individual transfer matrices of each layer:

$$\mathbf{T}_{\text{total}} = \mathbf{T}_n \cdot \mathbf{T}_{n-1} \cdot \ldots \cdot \mathbf{T}_1 \tag{2.78}$$

This total transfer matrix relates the fields at the beginning of the first layer to those at the end of the last layer.

From the total transfer matrix, physical quantities like the reflectance R and transmittance T of the entire stack can be calculated using the relations derived from the matrix components.

Chapter 3

Practical

(Comment: To demonstrate the simulation, all of the units on figures are ignored in this chapter, and I will continue with natural units.)

(Comment 2: Most of the plots are very computationally intensive. Thus, it is difficult to extend them to the large time limit. However, I feel like a lot of the plots illustrate the main purpose of this section quite well.)

3.1   1D Cavity Haloscope (Analytical Solutions)

3.1.1   Assumptions and conditions for the 1D case

In an experiment, when a magnetic field $\mathbf{B}$ is introduced in the presence of an axion field, an electric field $\mathbf{E}$ is induced parallel to $\mathbf{B}$. The axion field is described by a de Broglie wavelength λ_{dB} given by:

$$\lambda_{dB} = \frac{2\pi}{m_\phi v} \ , \tag{3.1}$$

where $v \approx 270$ kms^{-1} [8] represents the axion velocity, assuming $\hbar = 1$. For typical scenarios where the length scales of interest are much smaller than λ_{dB}, it's reasonable to assume that the gradient of the axion field $\nabla\phi \approx 0$, indicating a uniform field over small scales. The induced electric field $\mathbf{E}$ obeys the following equation of motion (recall the derivation from section 2.1),

$$\mu\epsilon\ddot{\mathbf{E}} = \nabla^2\mathbf{E} - \frac{\omega_\phi^2\mu}{Z_0}g_{\phi\gamma}\phi_0\mathbf{B}_e\cos\left(\omega_\phi t\right) \ . \tag{3.2}$$

Certain values of ω_ϕ would allow for resonance in the system; the resonance's intensity would depend on the cavity's size and $\mathbf{E}$. Within such a cavity, the modes of the electromagnetic field are quantised [11]

$$\mathbf{E} = \sum_{n=1}^{N} c_n\mathbf{E}(t) \tag{3.3}$$

$$c_n \propto \sin\left(\frac{n\pi x}{L}\right), \tag{3.4}$$

where L is the cavity's length and n is an integer. For these modes, the equation is simplified to

$$\nabla^2\mathbf{E} = -\frac{n^2\pi^2}{L^2}\mathbf{E} = -\omega^2\mathbf{E} \tag{3.5}$$

where the resonance with the applied electric is when $\frac{n\pi}{L} = \omega$.

In practical systems, losses from imperfect conduction in mirrors are significant. Therefore it is important to define a quality factor, Q, to represent the amount of energy "leaking" out

$$Q = \frac{\omega}{\Gamma}, \tag{3.6}$$

where Γ represents the loss rate, which is a constant in a uniform loss approximation.

3.1.2 Expectation for the 1D case

In one dimension, equation 3.2 can be simplified into the form of a driven harmonic oscillator, where the fields reside in a cavity with mirrors on both sides of the boundary

$$\ddot{E}(t) + 2\beta\dot{E}(t) + \omega_0^2 E(t) = j(t). \tag{3.7}$$

To solve equation 3.7, first define an inverse Fourier transform of the electric field and using properties from equations 2.25 to 2.27

$$\frac{1}{2\pi}\int \frac{d^2}{dt^2}\tilde{\phi}(\omega)e^{-i\omega t}d\omega + \frac{2\beta}{2\pi}\int \frac{d}{dt}\tilde{\phi}(\omega)e^{-i\omega t}d\omega + \frac{\omega_0^2}{2\pi}\int \tilde{\phi}(\omega)e^{-i\omega t}d\omega = \frac{1}{2\pi}\int j(\tilde{\omega})e^{-i\omega t}d\omega, \tag{3.8}$$

rewriting the left and right-hand sides as a function of ω and rearranging for $\phi(\omega)$

$$-\omega\tilde{\phi}(\omega) - 2\beta i\omega\tilde{\phi}(\omega) + \omega_0^2\tilde{\phi}(\omega) = \tilde{j}(\omega), \tag{3.9}$$

$$\tilde{\phi} = \frac{\tilde{j}(\omega)}{-\omega^2 - 2\beta i\omega + \omega_0^2}. \tag{3.10}$$

Now, consider a sinusoidal driving frequency for this system, represented by $j(\omega) = A\cos(\Omega t)$, the Fourier transform would be

$$\tilde{j}(\omega) = \frac{2\pi A}{2}(\delta(\omega - \Omega) + \delta(\omega + \Omega)), \tag{3.11}$$

substituting into the Fourier transform of $\phi(t)$

$$
\begin{aligned}
\phi(t) &= \frac{1}{2\pi}\int \tilde{\phi}(\omega)e^{-i\omega t}d\omega \\
&= \frac{1}{2\pi}\int \left(\frac{\tilde{j}(\omega)}{-\omega^2 - 2\beta i\omega + \omega_0^2}\right)e^{-i\omega t}d\omega \\
&= \frac{1}{2\pi}\int \left(\frac{1}{-\omega^2 - 2\beta i\omega + \omega_0^2} \times \frac{2\pi A}{2}(\delta(\omega - \Omega) + \delta(\omega + \Omega))\right)e^{-i\omega t}d\omega \\
&= \mathrm{Re}\left[e^{-i\Omega t}\frac{-A}{\Omega^2 + 2i\beta\Omega - \omega_0^2}\right].
\end{aligned}
\tag{3.12}
$$

From equation 3.12, when $\omega_0 = \Omega$, the external field is driving at the natural frequency; thus $\phi(t)$ would return

$$\phi(t) = \frac{A}{2\beta\omega_0}\sin(\omega_0 t). \tag{3.13}$$

The power exerted by the driving frequency is force times velocity

$$
\begin{aligned}
P(t) &= j(t)\dot{\phi}(t) \tag{3.14} \\
&= \frac{A^2}{2\beta}\cos(\omega_0 t) \\
&= \frac{A^2}{4\beta}[1 + \cos(2\omega_0 t)], \tag{3.15}
\end{aligned}
$$

the value of $P(t)$ is always positive due to the definition of resonant frequency, where the work done by the external field is always positive. The power loss can also be found through

$$\langle P_{\mathrm{loss}}\rangle = \frac{\omega_0}{2\pi}\int P(t)dt. \tag{3.16}$$

3.1.3   General output for the 1D case

The simulation of the 1D cavity haloscope would be using equation 3.7, with a slight change of variables

$$\ddot{\phi}(t) + \gamma\dot{\phi}(t) + \omega_0^2\phi(t) \approx \frac{\mu}{Z_0}g_{\phi\gamma}\phi_0 B_e \cos(\omega_\phi t). \tag{3.17}$$

Rewrite the constants on the right hand side such that $\phi(t)\left[Z_0/(\mu g_{\phi\gamma}\phi_0 B_e)\right] = \psi(t)$

$$\ddot{\psi}(t) + \gamma\dot{\psi}(t) + \omega_0^2\psi(t) = \cos(\omega_\phi t). \tag{3.18}$$

The boundary conditions to solve this equation are given as

$$\psi(t=0) = 0 \quad \dot{\psi}(t=0) = 0. \tag{3.19}$$
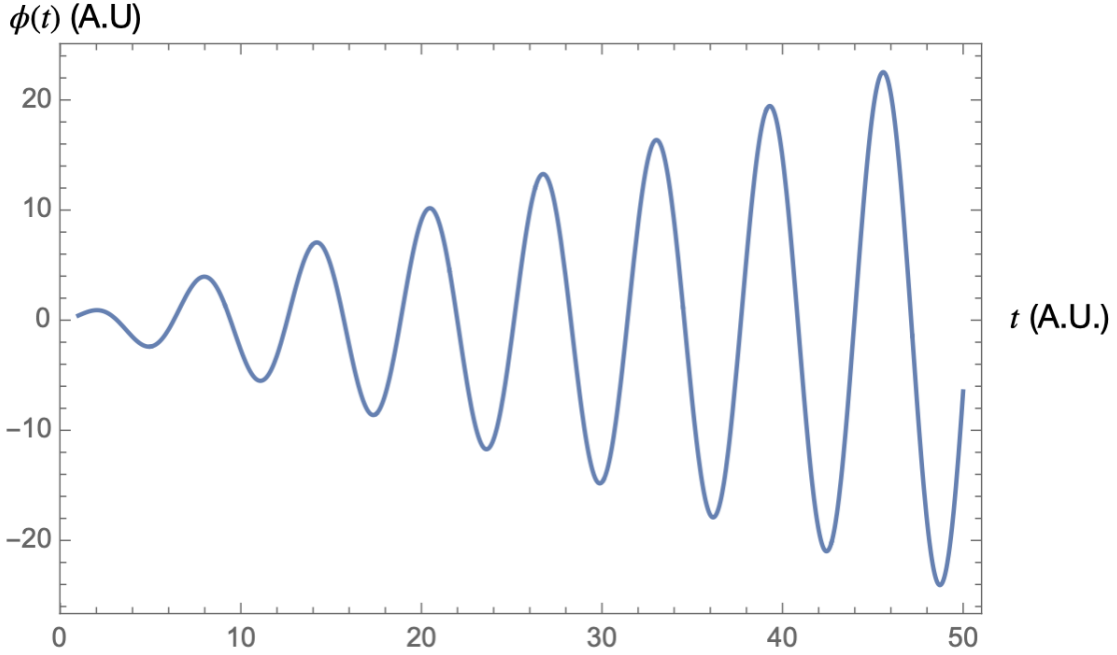
Figure 3.1: The solution for $\phi(t)$ with some additional driving current, for a small enough γ and with the appropriate ω_ϕ and ω, resonance of $\phi(t)$ would become apparent; $\gamma = 0.001$ and $\omega = \omega_\phi = J = 1$. From the image, it can be seen that there is a resonance between the axion-induced field and the applied electric field; from the definition of resonance being positive work done, it is seen that the amplitude of the field is increasing at every cycle.

Eventually, the plot of Figure 3.1 would reach a steady state (this is shown in Figure 3.4); therefore, we can use this knowledge to verify whether or not the chosen ω_ϕ would truly resonate with the applied field (Theoretically it should be, but numerical simulations could contain errors, thus instead of $\omega_\phi = 1$, it could be $\omega_\phi = 1.000\ldots01$, for small values it would be undetectable, much we are dealing with an order of magnitude of $\approx 10^{-35} - 10^6 - 10^{22}$), additionally it can provide some intuition for how precisely the detection equipment's are required to be as a minor variation could significantly reduce the detectable power; shown in figure 3.2 is the result of varying the frequency of the applied field, while figure 3.3 is the power loss, plotted using equation 3.16.
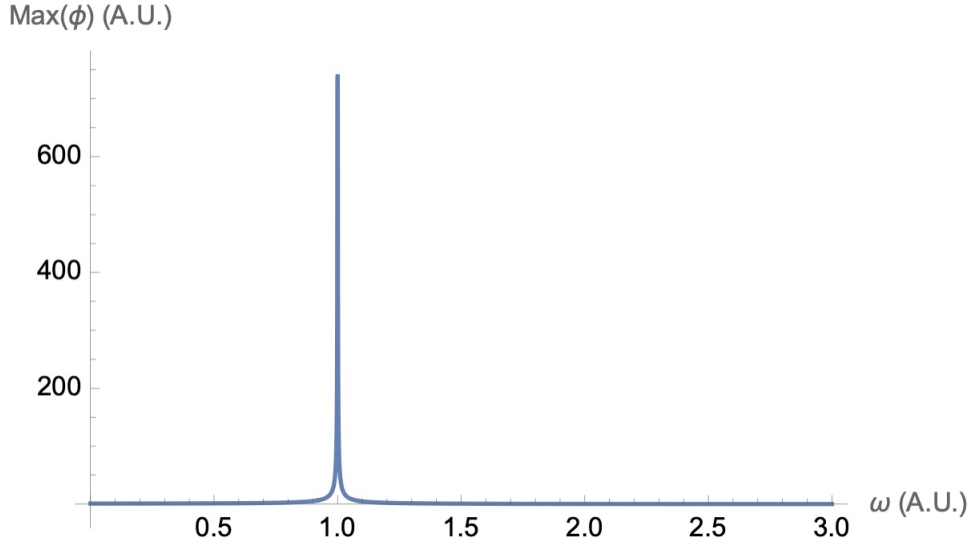
Figure 3.2: A scan of ω values, to confirm if the value chosen in figure 3.1 represents the maximum possible resonance; $\text{Max}(\phi(t))$ is the maximum value that $\phi(t)$ could reach for an arbitrarily long amount of time; the amplitude of $\phi(t)$ in a small time frame, relative to γ, would appear to be linearly increasing; but for long time frames, the amplitude would remain constant.
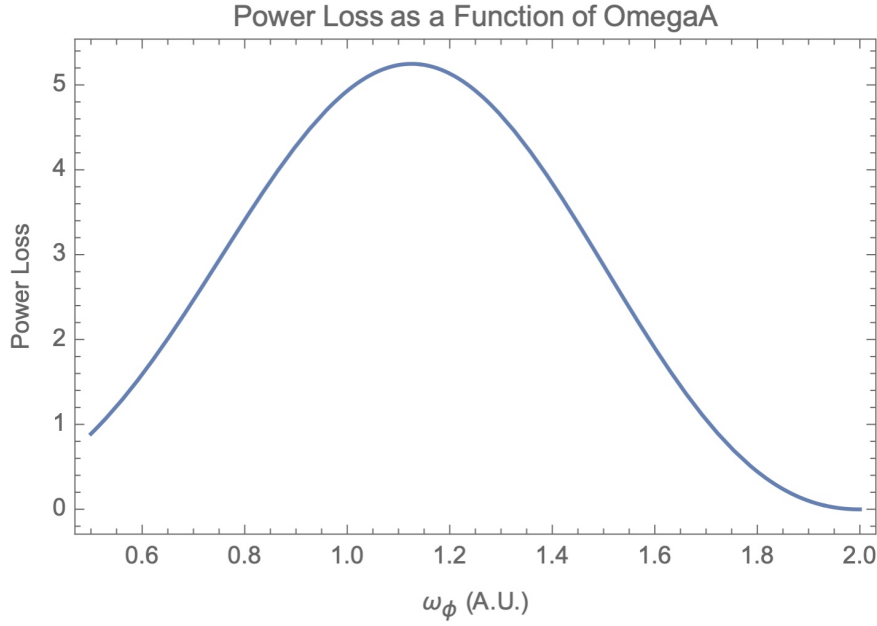

Figure 3.3: A plot of equation 3.16, where $P(t) = j(t)\dot{\psi}(t)$, and $\dot{\psi}(t)$, is obtained through the numerical simulation of equation 3.18. The power loss curve correlates with Figure 3.2, which is expected that when the axion-induced field resonated with the applied field strongly, the resultant power loss would be higher. This is a method to detect the existence of dark matter; instead of having a detector within the cavity, it can exist on the outer surface and detect the increases in power loss.
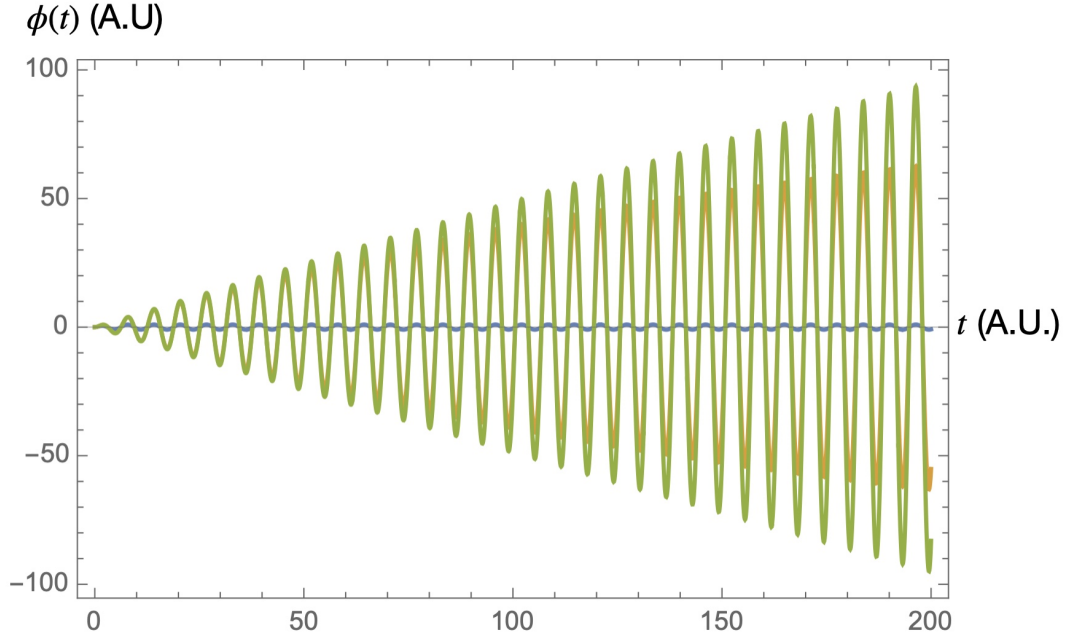
Figure 3.4: A plot of blue, orange and green with $\gamma = 1, 0.01, 0.001$ respectively. You can see that the blue curve reached its steady state nearly instantly due to the large damping factor, thus showing that the resonance does not overcome a large γ factor; however, a reduction in the γ factor would greatly increase the amplitude of $\phi(t)$, a decrease of γ by a factor of 10 would increase the amplitude by a factor of 50 (not accounting for units). We can also see that the orange curve is reaching its steady state, thus verifying our reasoning for the plot of Figure 3.2

3.2 2D Circular Boundary Condition (Numerical Solutions)

For the 2D case, we directly work with equation 3.2. Firstly, circular boundary conditions are defined (the numerical solution would be complicated to solve in non-polar/cylindrical coordinates). Define $r = \sqrt{x^2 + y^2}$ for some arbitrary circle size. We will still be working functions of x, y and setting the constants equally to one thus equation 3.2 would be represented as

$$\ddot{\mathbf{E}} = \nabla^2 \mathbf{E} - \frac{\omega_\phi^2 \mu}{Z_0} g_{\phi\gamma} \phi_0 \mathbf{B}_e \cos(\omega_\phi t) \tag{3.20}$$

$$\ddot{\mathbf{E}}' = \nabla^2 \mathbf{E}' - \omega_\phi^2 \cos(\omega_\phi t), \tag{3.21}$$

with boundary conditions that satisfy an initial value problem

$$E(x, y, t = 0) = 0 \qquad \partial_t E(x, y, t)|_{t=0} = 0 \qquad E(r_{\max}, t) = 0, \tag{3.22}$$

the physical intuition of these boundaries can be viewed as some initial excitation and $x, y = 0$ and $t = 0$, then we also enforce that the wave disappears that the boundary $r_{\max}$, thus presenting the solution of $\mathbf{E}'$ in figure 3.5 and 3.6. But first, let's discuss the general case of a 2D cavity, and we can compare it to the numerical results; in [11], a general form of the electric field is given interns of the Bessel function, where resonance happens at the first root [14]; therefore we are interested in the TM$_{nlm}$ where $n = 0, l = 1, m = 0$,

$$E_z(r, \phi, z, t) = E(t) J_m\left(\frac{x_{ml}}{R} r\right) e^{\pm im\phi} \cos\left(\frac{n\pi z}{L}\right) \tag{3.23}$$

$$E_z(r, \phi, z, t) = E(t) J_0\left(\frac{x_{01}}{R} r\right) e^{\pm im\phi} \tag{3.24}$$

Returning to figure 3.5 and 3.6, it is important to observe if the propagation resembles some form of the Bessel function, where the resonance happens at the first root.
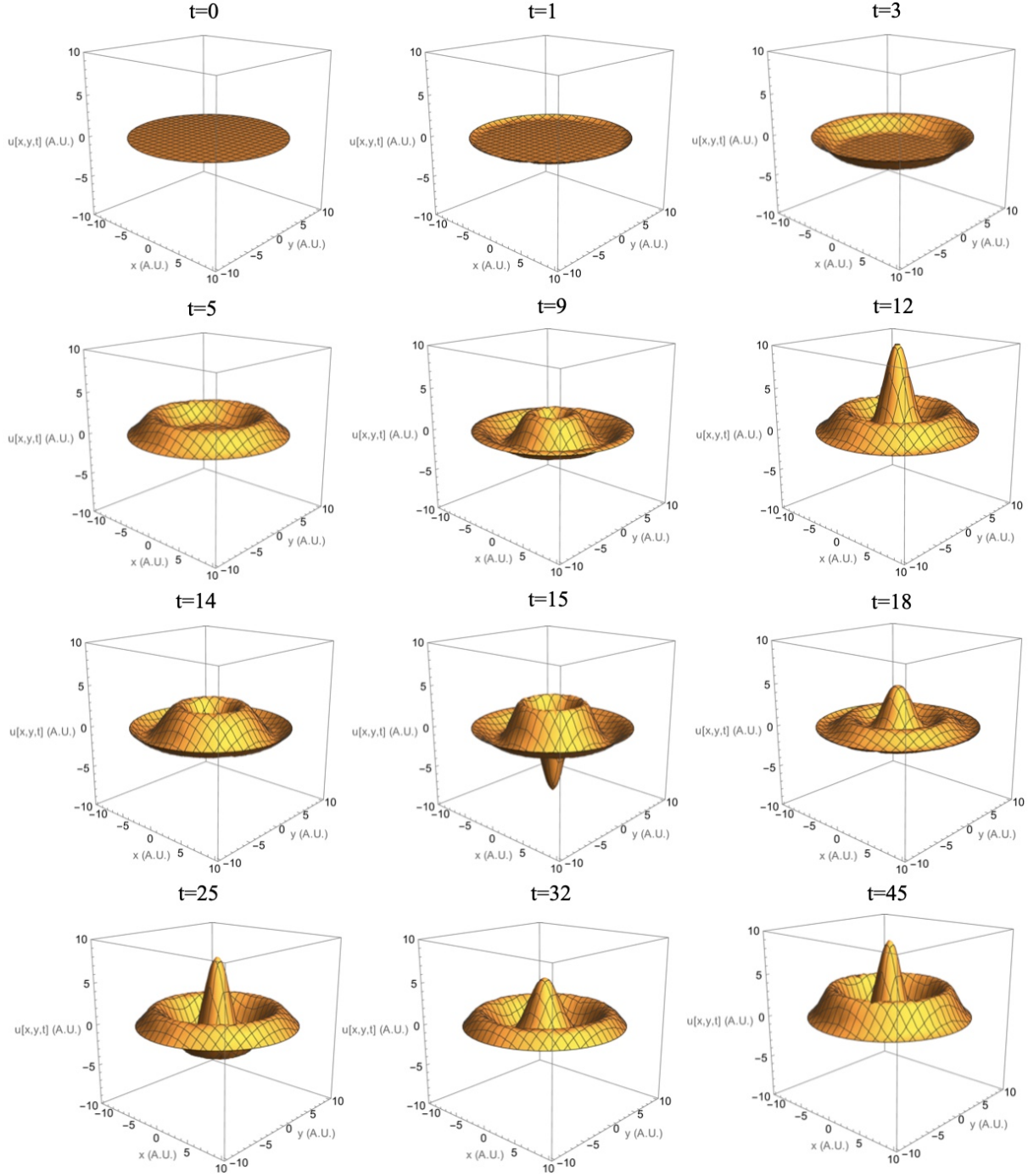
18

Figure 3.5: In the original code, this is an animation to show the change in the value of $E'(x, y, 0 \leq t \leq 50)$ (In the images, it is represented as $u[x, y, t]$), due to certain limitations, 12 snapshots had been taken to accurately depict the propagation of the amplitude of the electric field with an axion-induced driving field. The images chosen from $t = 0$ to $t = 18$ provide an intuition for how the field would vary; initially, at $t = 0$, the amplitude is zero, and as the field varied, x, y at $r_{\max}$ is also zero, both of these situations satisfied equation 3.22. Additionally, notice how the maximum value of the electric is shown at the first peak, i.e. the first peak is at $t = 12$, additional peaks are present at $t = 25, 32, 45$, but the maximum value started to decrease.

19

Now that we have seen a 3D representation of the amplitude of the arbitrary field, know that it satisfied relevant experimental boundary conditions, and we know that the field has rotation symmetry based on Figure 3.5. Thus it is reasonable to look at a cross-section with no loss of information.
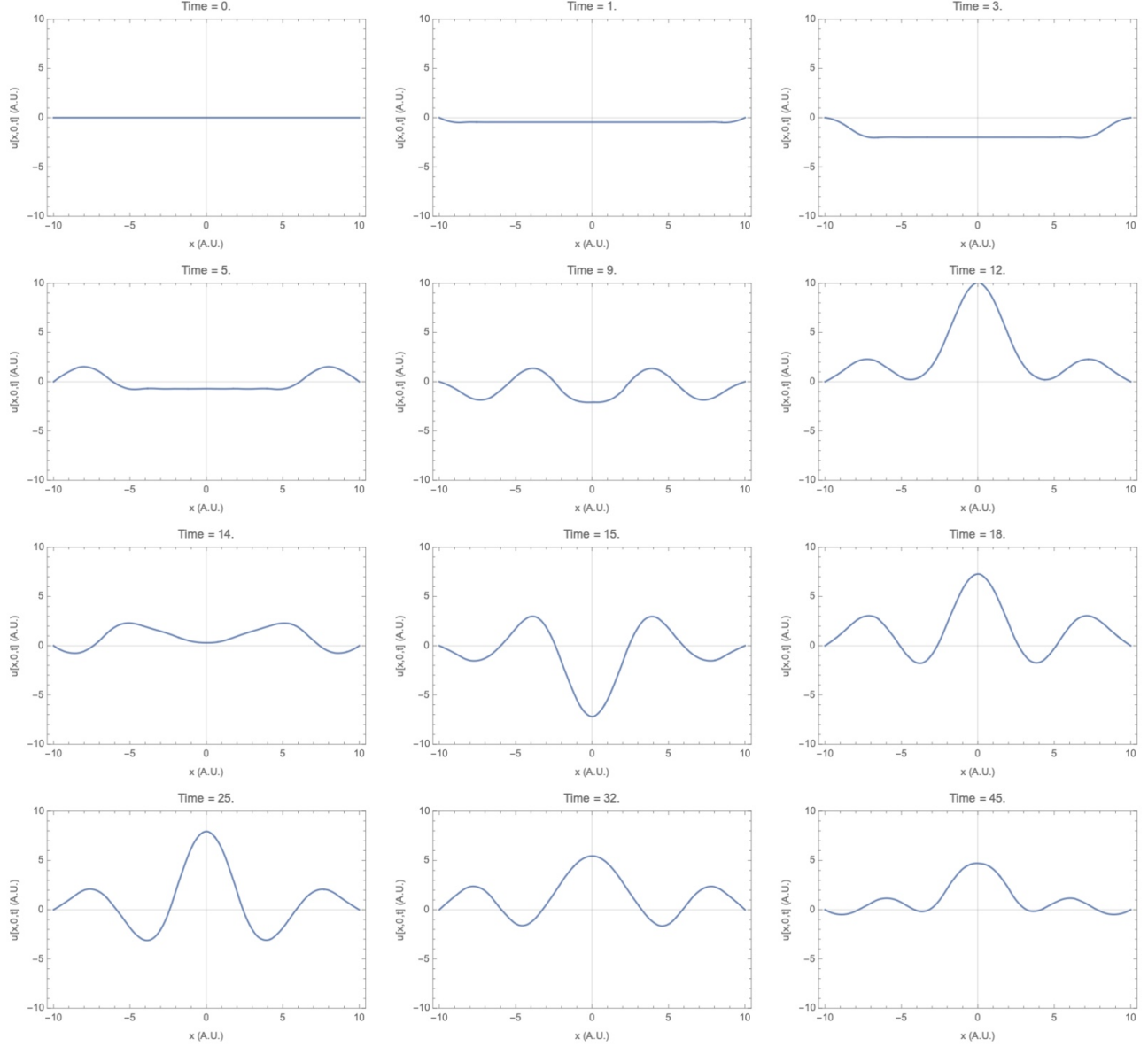

Figure 3.6: A cross section, by setting $y = 0$, with the same time sets as figure 3.5. From the 2D representation, we can immediately see the boundary conditions being satisfied, and additionally, at $t = 12, 18, 25, 32, 45$, the graphs resembled the first, second and third roots of J_0. Therefore the results could be a solution for the resonance of an axion-induced field with an applied electric field.

We know from Figure 3.6 that the numerical result is a potential solution for resonance; thus, we are interested in maximising this resonance, i.e. we don't want the second, third, fourth, n^{th}, roots of the Bessel function, we are only interested in the first root. From [2], Feynman provided a formula to calculate the radius of resonance for a cylindrical can

$$\omega_0 = 2.405\frac{c}{r}. \tag{3.25}$$

Exploring around equation 3.25, and plotting the values of $E(x = 0, y = 0, t)$ (observe from figure 3.5, when $x = 0$ and $y = 0$, we are just observing the change in the the electric field) for different radius, we see from figure 3.7 how the electric field would vary.
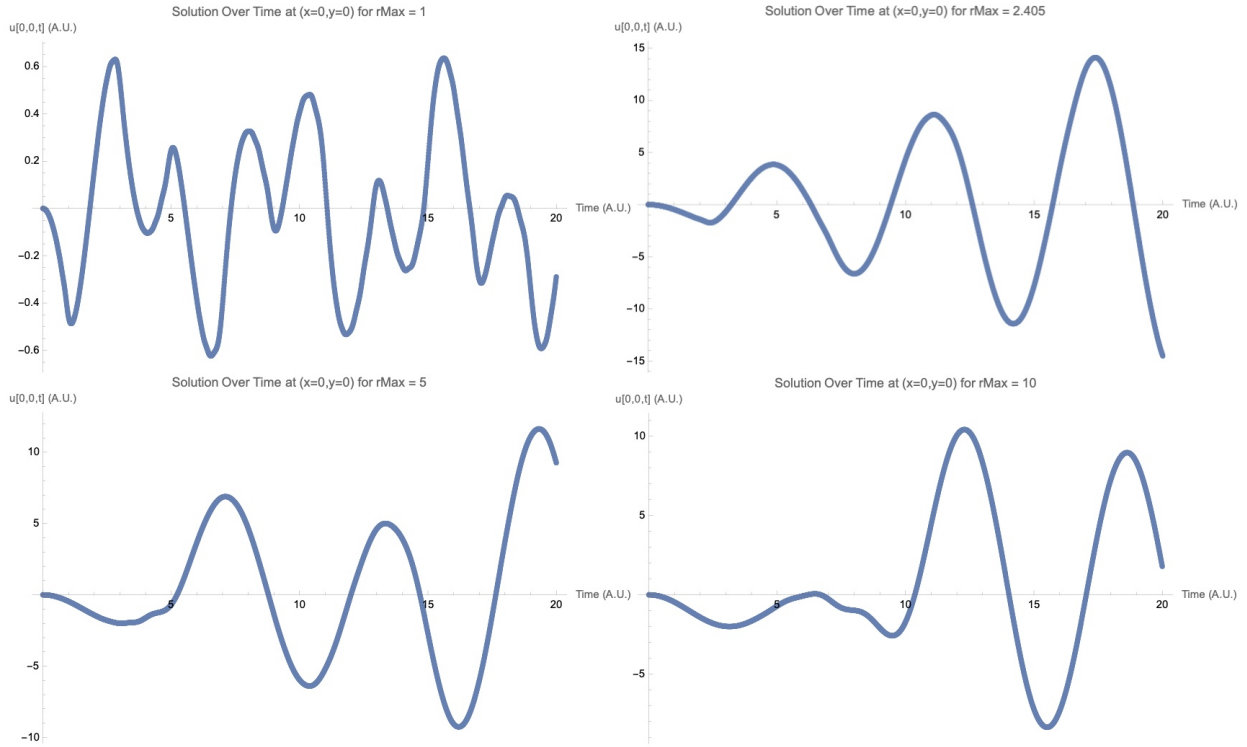

Figure 3.7: Four plots, when $r_{\max} = 2.405$ and three other plots to explore around the value of $r_{\max}$. We can see no resonance in the top left graph, and some form of resonance is present in the bottom right graph (but it quickly reached the steady state/ potentially reduced in amplitude). The top right figure shows clear resonance, which resembles figure 3.1 in the 1D case (which we know is a solution to resonance). Thus, this figure quite confidently supports a solution for resonance in a 2D cylindrical boundary.
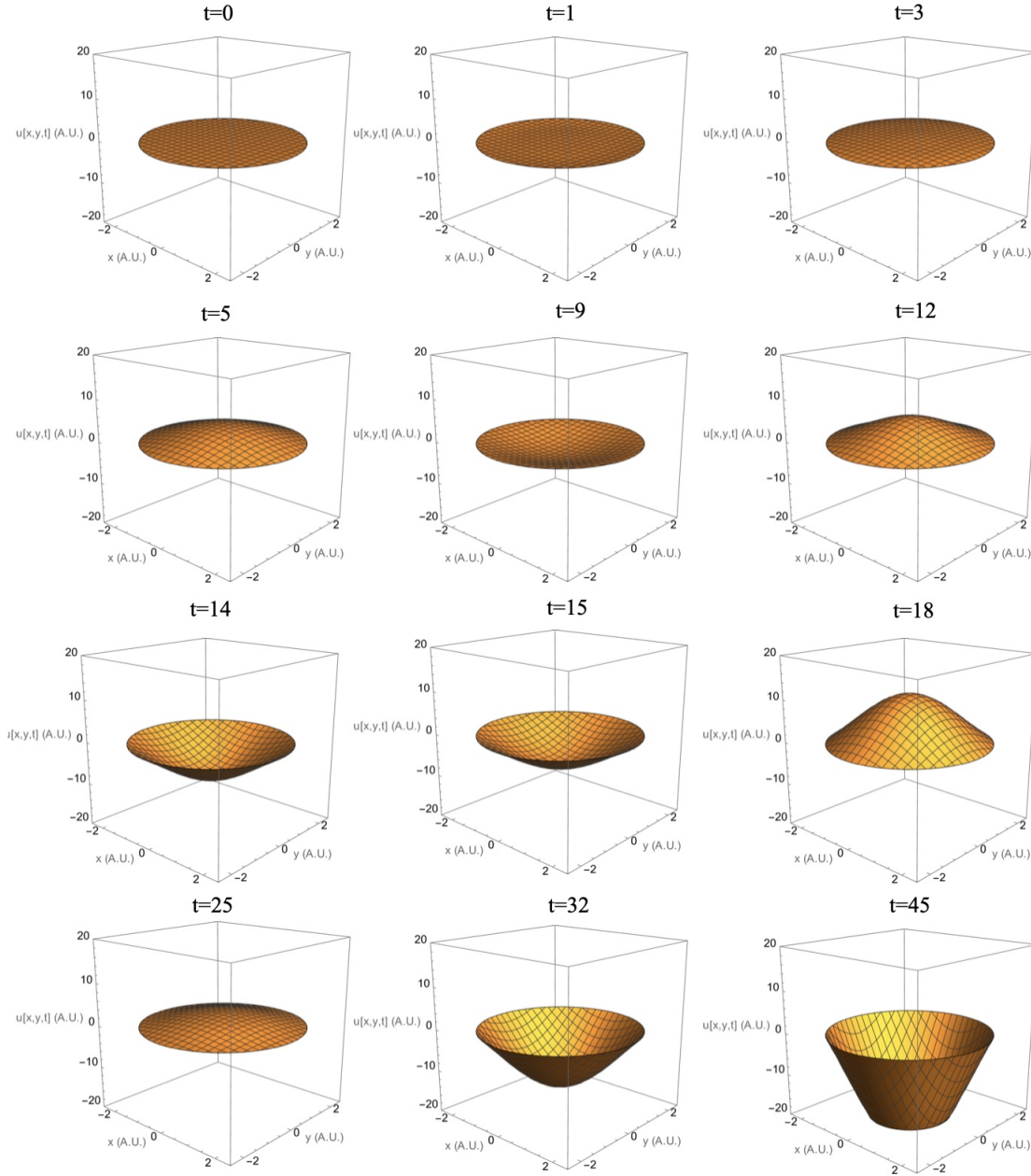
Figure 3.8: A plot of figure 3.7 top right, for $r_{\max} = 2.405$. The plot starts off with a small amplitude for the electric field, then progresses and grows, oscillating about its centre; this is a representation of the first root of the Bessel function, with boundary solutions from equation 3.22; these plots are a 2D representation for figure 3.1
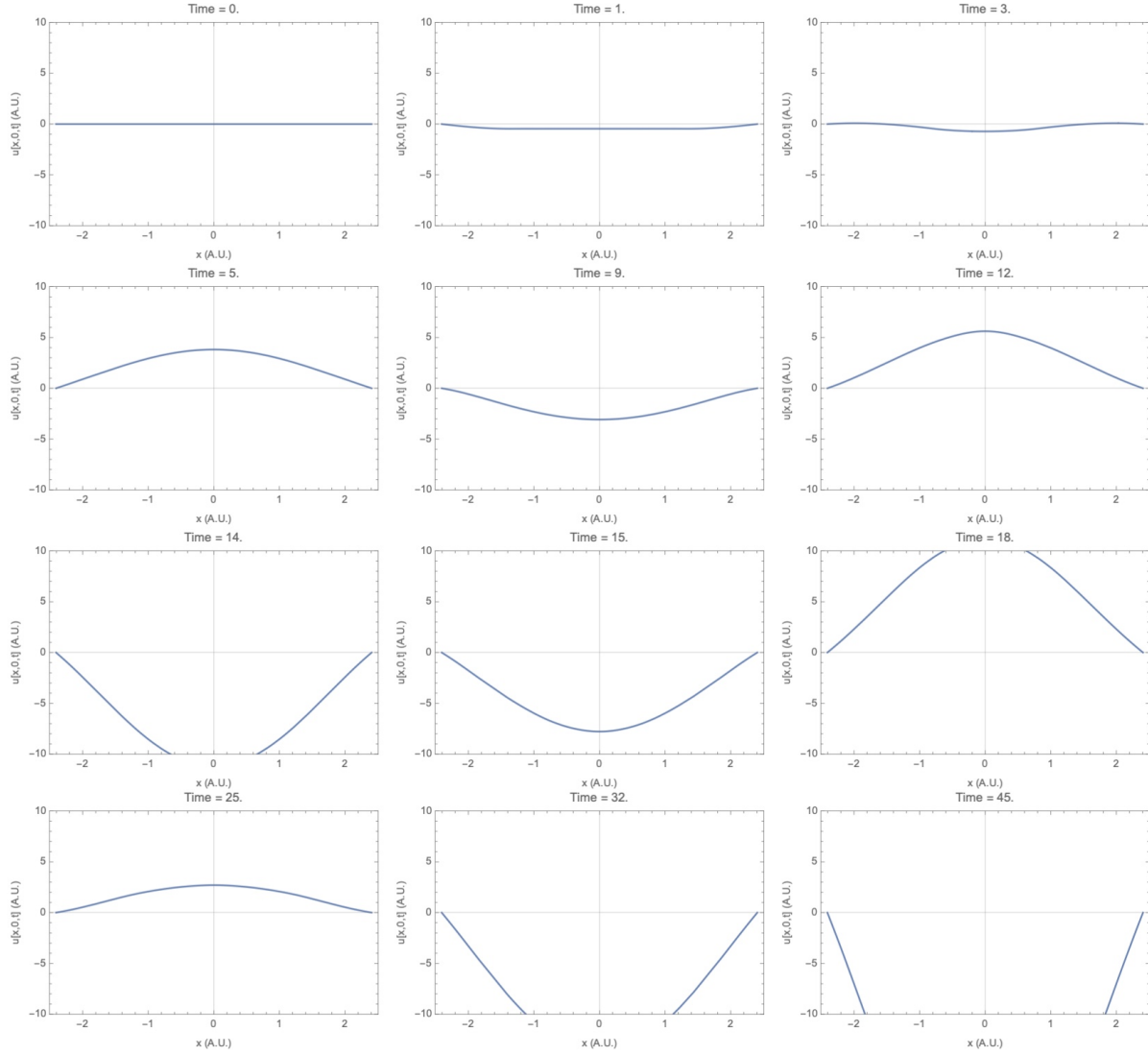
Figure 3.9: Like figure 3.6, the plots shown here are more obvious in their resonance, again no loss of information due to the symmetry of figure 3.8

Chapter 4

Results

4.1 Known Results from Simulations

This section is to present the results for the cavity haloscope, from [4]. In the paper titled "Simulation of classical axion electrodynamics using comsol multiphysics", figure 4.1 was their result, the software called comsol; thus, with the numerical simulations from section 3, we will try to include units into the simulation and reproduce non-arbitrary results.
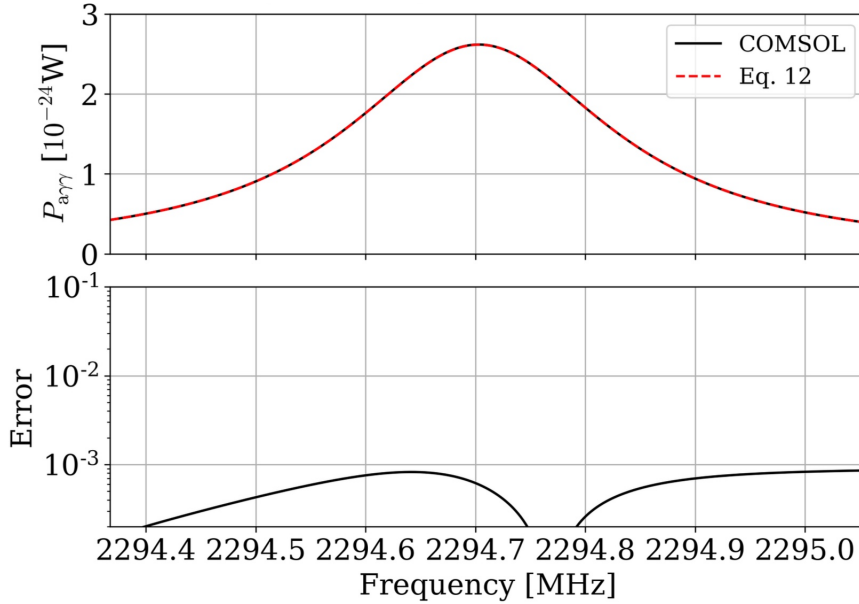

Figure 4.1: Conversion power obtained for near resonance interaction between axion-induced field and applied electric field; assumed local dark matter composed solely by the KSVZ axion [7]. (Figure from [4])

The Axion Dark Matter eXperiment (ADMX) aims to detect cold dark matter axions directly. The experiment explores the mass range of approximately μeV to meV while focusing on detecting axions. This is achieved by using a haloscope designed to resonate and increase the number of photons produced by axion decay in a strong magnetic field within a microwave cavity. Previous reports by ADMX have excluded masses in the range 2.7–3.3μeV for the DFSZ model. By the year 2021, ADMX reported the results of the search and exclusion for axions in the 3.3–4.2μeV mass range [5]. ADMX can tune the TM$_{010}$ mode from 500MHz to 900MHz [1].

4.1.1 Overlap Integral Formalism

The method to calculate the power for cavity haloscopes is through the use of overlap integrals [12]. The reacted field and conversion power near resonance are approximated by

$$\mathbf{E}_r \approx \mathbf{E}_m + \frac{g_{\phi\gamma}\phi_0}{\sqrt{\epsilon\mu_0}\mathbf{B}_0}, \tag{4.1}$$

$$P_{\phi\gamma} \approx \left[\frac{g_{\phi\gamma}^2 \rho_\phi}{m_a^2 c/\hbar^3}\right]\left[\omega_\phi \int \mu^{-1}|\mathbf{B}|^2 dV_c\right] \times \tag{4.2}$$

$$C\frac{Q_c Q_a}{Q_c + Q_a}\frac{1}{((2Q_c(\omega_\phi - \omega_c)/\omega_c)^2 + 1)}, \tag{4.3}$$

where $\mathbf{E}_m$ is the reacted electric field forming the modes of the cavity, while $Q_{c,\phi}$ are the quality factors of the cavity and axion, and C is a unit-less form factor, representing how well the electric field is aligned with the magnetic field

$$C = \frac{\left|\int \mathbf{E}_r \cdot \mathbf{B}_0 dV_c\right|^2}{\int \epsilon_r |\mathbf{E}_r|^2 dV_c \int |\mathbf{B}_0|^2 dV_c}. \tag{4.4}$$

4.2 Simulation results and comments on accuracy

Figure 4.2 is meant to be a reproduction of figure 4.1; the shape of the curve is quite accurate, as they are both a Gaussian-like shape for a small deviation in the frequency; additionally, for a large range of frequencies, they are both a peak. However, due to certain conversion and simulation errors, the power output is not exactly aligned, with Figure 4.2 being off by a factor of four; a factor of four might appear to be quite a large error, but the numerical values are of order 10^{-15}, to 10^{16}; thus a factor of four would be quite likely with some small calculation and or approximations.
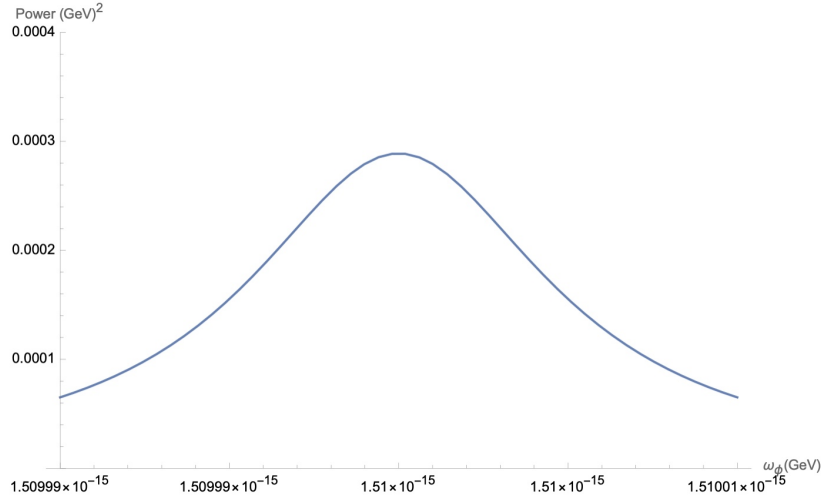

Figure 4.2: Applying equations 4.1 to 4.4, with dimensionally consistence units: ω_c, Q_c, r, z, n, l, m, $g_{\phi\gamma}$, ρ_ϕ, m_ϕ and B_e ; with their respective values: $1.51 * 10^{-15}$, 140000, 0.05, 0.1, 0, 1, 0, 0.97,450000, $3.4671 * 10^{-4}$, 10. The final result is around $2.8 * 10^{-4}\text{GeV}^2$, converting from natural units, it is around $1.13 * 10^{-32}$Watts, this is quite a few orders of magnitude of the result from comsol
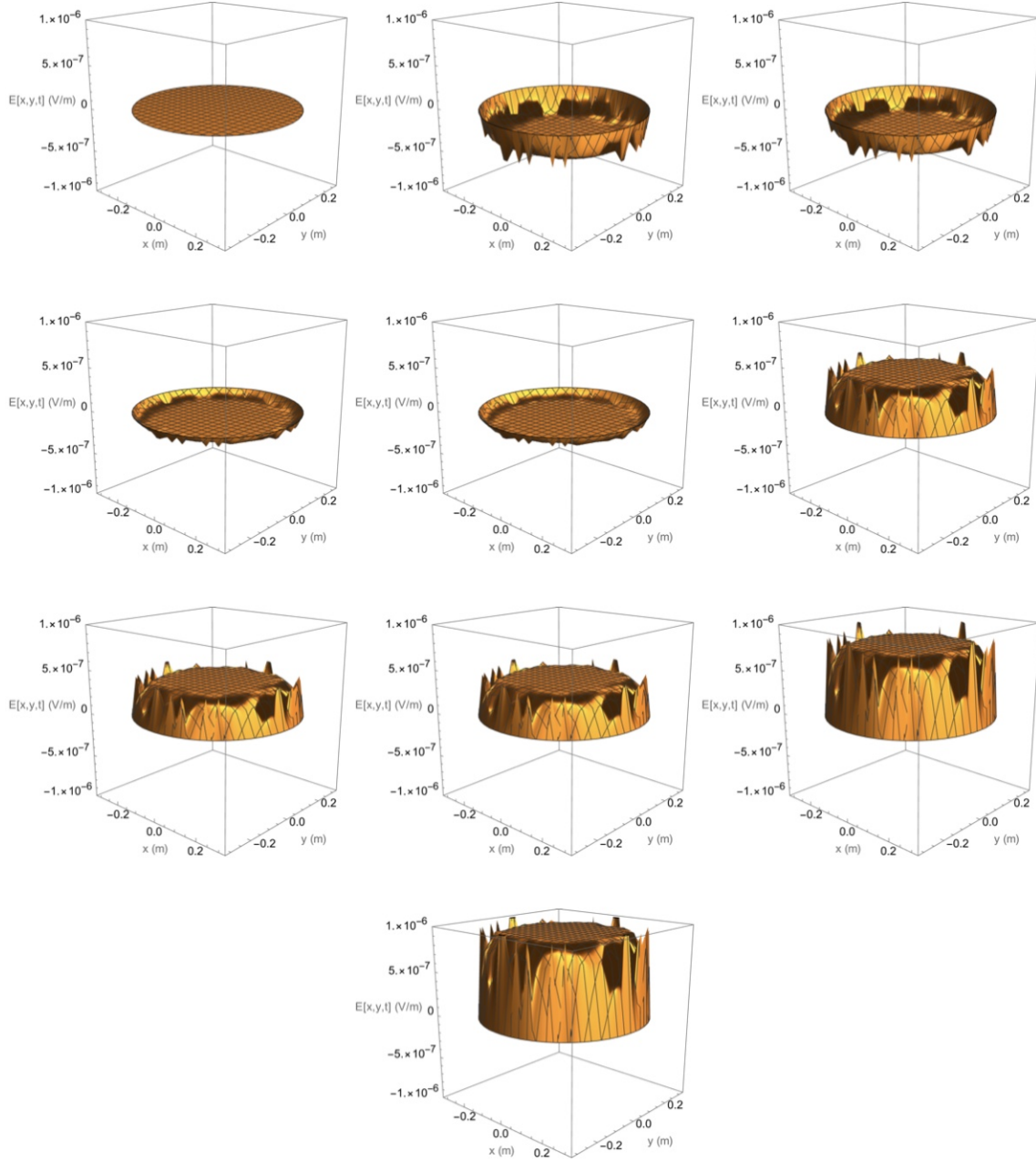
Figure 4.3: These figure are from $t = 0$ to $t = 0.01s$ with a $t = 0.001s$ time step. Substituting in the values of $\omega = 2295$MHz, and $\mu g_{\phi\gamma}\phi_0 \mathbf{B}_e/Z_0$, which is equal to 3.33×10^{-29} and with units of $T\ s/m$. However, the resultant value is much higher than what we are expecting, with some initial variation of $\pm 3 \times 10^{-7} V/m$ and progressing up to $5 \times 10^{-7} V/m$. From section 2.2.2, the electric field of dark matter is expected to be around $9.7 \times 10^{-12} V/m$. Therefore, it is unlikely that the electric field strength would increase substantially within a range of $t = 0.005s$. However, we can see that the simulation still obeyed the initial conditions while producing resonance.
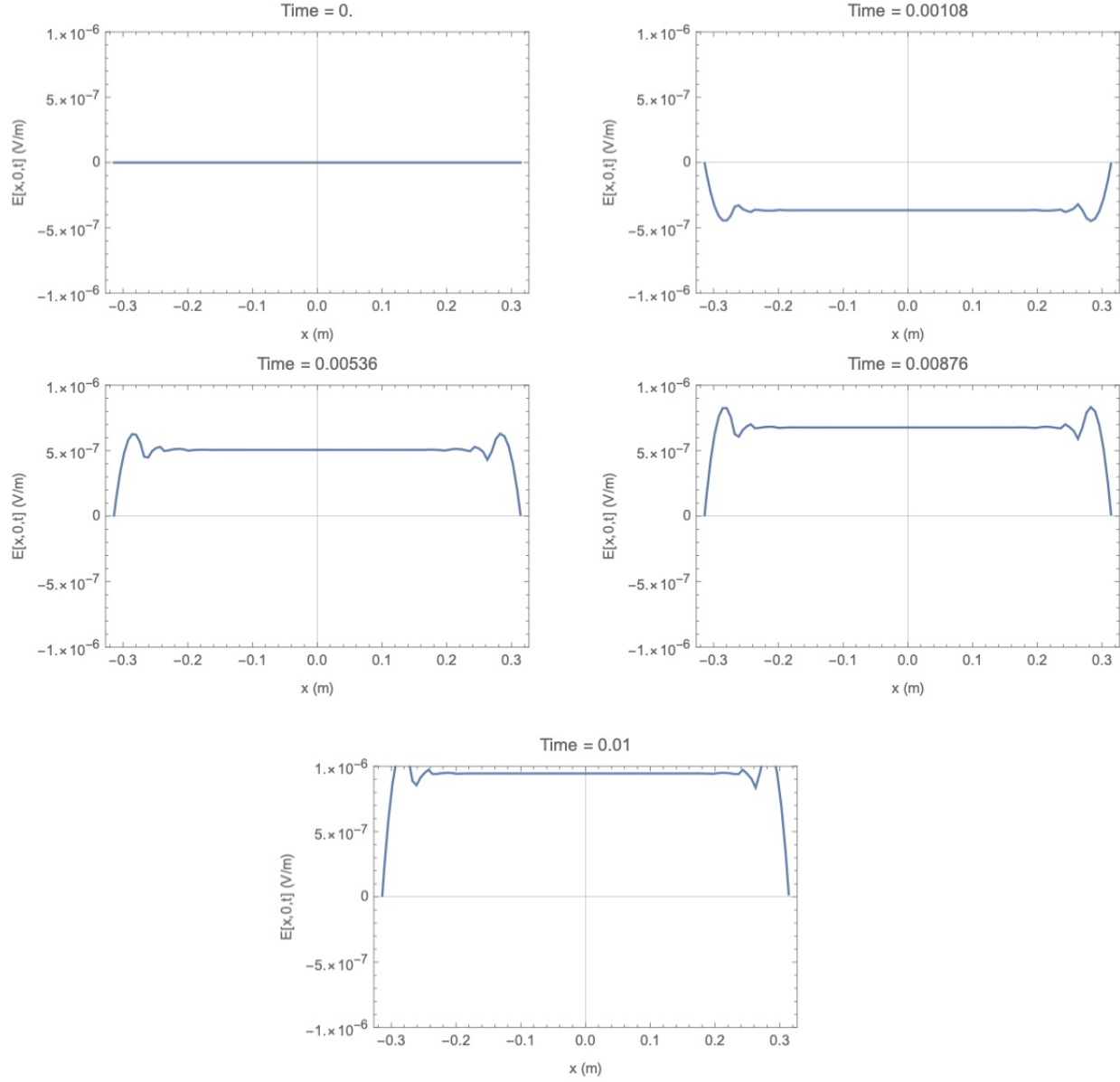
Figure 4.4: A cross-section of figure 4.3, here we can see much more clearly how the amplitude changes; it starts off with some small oscillation, and as the axion-induced field begins to interact with the applied electric field, the amplitude starts to pick up, producing a resonance much like figure 3.9

The numerical results were not very accurate. However, it is essential to note that the physics still makes sense, and figures 4.2 to 4.4 are still representative of the interaction described in chapter 3. Thus, it could very well be some mistake in conversion, a lack of computational power, or overflowing of decimals in Mathematica; for example, $1/\alpha$ where for $\alpha \approx 10^{30}$, to do calculations and numerical simulations would result in the system approximating $1/\alpha \approx 0$. Thu certain liberates had to be taken in order to get any visible results.
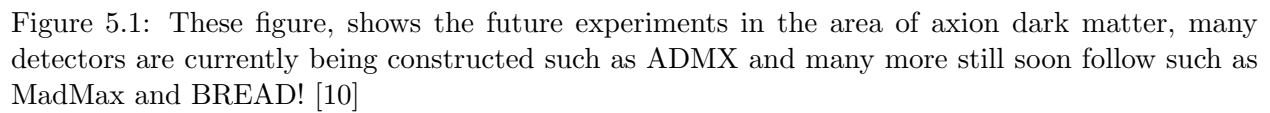
Chapter 5

Conclusion and Future Outlooks

In this thesis, the theoretical explanation of dielectric and cavity haloscopes has been covered. Additionally, certain novel results had been derived, starting from the axion-Maxwell's equations derived from the QCD Lagrangian; an approximation of cold dark matter had been made to simplify the axion-Maxwell's equations into a simpler form; this new form could be substituted into one another to derive the wave equation with an axion-induced field. Returning to the original form of the axion-Maxwells's equations, we proceeded to linearised them by using the $\mathbf{D}$ and $\mathbf{H}$ fields and apply a Fourier transform such that they become the macroscopic axion-Maxwel's equations in Fourier space. Afterwards, the expected electric field strength of the axion was calculated, and some intuitions for its size were given. In section 2.2.3, an argument for the dielectric conditions to be satisfied would require that the axion field not be treated as a stationary field; with this realisation, the Poynting vector was derived with the addition of the axion field. Finally, in Chapter 2, we also covered an alternative method to approach dielectric called transfer matrix.

In Chapter 3, the theory and arguments for the numerical simulations were given, first starting off with the 1D cavity haloscope, then expanding up to 2D; this could be a potential future outlook where simulation on 3D haloscopes and optimising the structure of the detection for better output. The numerical simulation of the physics for 1D and 2D was very successful, as it reproduced what was expected to happen during a resonance between the axion field and the applied electric field. However, when the units and numerical values were included, the simulation still retained the physics, but the numerical values delivered were a few orders of magnitude off, which could be due to a mistake in conversion, a lack of computational power, or overflowing of decimals in Mathematica. Thus, in the future, perhaps a more robust system could be coded such that it produces more accurate results relative to the experimental observations.

There are also additional issues, for example, in 2.2.4 we ignored the electric field close to the dielectric, where the interaction between the H, B and E-field, would become too complicated. Thus, I would be interested in performing a more realistic experiment simulation on the physics behind the axion-induced electric field with an applied electric field; perhaps this progress would offer a more concrete formulation for the numerical results. Thus, it could resemble the experimental results.

Figure 5.1: These figure, shows the future experiments in the area of axion dark matter, many detectors are currently being constructed such as ADMX and many more still soon follow such as MadMax and BREAD! [10]

Bibliography

[1] S. J. Asztalos, G. Carosi, C. Hagmann, D. Kinion, K. van Bibber, M. Hotz, L. J. Rosenberg, G. Rybka, J. Hoskins, J. Hwang, P. Sikivie, D. B. Tanner, R. Bradley, and J. Clarke. Squid-based microwave cavity search for dark-matter axions. *Physical Review Letters*, 104(4), Jan. 2010.

[2] R. Feynman. The feynman lectures on physics. *Caltech's Division of Physics, Mathematics and Astronomy*, 1963.

[3] I. Irastorza, S. Cebrián, E. García, D. González, A. Morales, J. Morales, A. Ortiz de Solórzano, A. Peruzzi, J. Puimedón, M. Sarsa, S. Scopel, and J. Villar. Prospects for solar axion searches with crystals via bragg scattering. *Nuclear Physics B - Proceedings Supplements*, 87(1–3):102–104, June 2000.

[4] J. Jeong, Y. Kim, S. Bae, and S. Youn. Simulation of classical axion electrodynamics using comsol multiphysics. *Journal of the Korean Physical Society*, 83(3):161–167, Apr. 2023.

[5] R. Khatiwada, D. Bowring, A. S. Chou, A. Sonnenschein, W. Wester, D. V. Mitchell, T. Braine, C. Bartram, R. Cervantes, N. Crisosto, N. Du, L. J. Rosenberg, G. Rybka, J. Yang, D. Will, S. Kimes, G. Carosi, N. Woollett, S. Durham, L. D. Duffy, R. Bradley, C. Boutan, M. Jones, B. H. LaRoque, N. S. Oblath, M. S. Taubman, J. Tedeschi, J. Clarke, A. Dove, A. Hashim, I. Siddiqi, N. Stevenson, A. Eddins, S. R. O'Kelley, S. Nawaz, A. Agrawal, A. V. Dixit, J. R. Gleason, S. Jois, P. Sikivie, N. S. Sullivan, D. B. Tanner, J. A. Solomon, E. Lentz, E. J. Daw, M. G. Perry, J. H. Buckley, P. M. Harrington, E. A. Henriksen, K. W. Murch, and G. C. Hilton. Axion dark matter experiment: Detailed design and operations. *Review of Scientific Instruments*, 92(12), Dec. 2021.

[6] Y. Kim, D. Kim, J. Jung, J. Kim, Y. C. Shin, and Y. K. Semertzidis. Effective approximation of electromagnetism for axion haloscope searches, 2019.

[7] T. Li. The ksvz axion and pseudo-nambu-goldstone boson models for the xenon1t excess, 2020.

[8] D. J. E. Marsh, D. Ellis, and V. M. Mehta. *Dark Matter: Evidence, Theory, and Constraints.* Princeton University Press, 2024.

[9] A. J. Millar, G. G. Raffelt, J. Redondo, and F. D. Steffen. Dielectric haloscopes to search for axion dark matter: theoretical foundations. *Journal of Cosmology and Astroparticle Physics*, 2017(01):061–061, Jan. 2017.

[10] C. O'Hare. cajohare/axionlimits: Axionlimits. `https://cajohare.github.io/AxionLimits/`, July 2020.

[11] C. A. O'Hare and A. M. Green. Axion astronomy with microwave cavity experiments. *Physical Review D*, 95(6), Mar. 2017.

[12] P. Sikivie. Invisible axion search methods. *Rev. Mod. Phys.*, 93:015004, Feb 2021.

[13] L. L. Sánchez-Soto, J. J. Monzón, A. G. Barriuso, and J. F. Cariñena. The transfer matrix: A geometrical perspective. *Physics Reports*, 513(4):191–227, Apr. 2012.

[14] Wikipedia contributors. Bessel function — Wikipedia, the free encyclopedia, 2024. [Online; accessed 26-April-2024].